Abstract

Title of thesis: AN IMAGE-BASED APPROACH FOR TRACKING HELICOPTER LONGITUDINAL TIP-PATH-PLANE ANGLE

Richard Sickenberger, Master of Science, 2008

Thesis directed by: Dr. Fredric H. Schmitz

Department of Aerospace Engineering

An optics-based longitudinal tip-path-plane measurement system has been designed and flown onboard a Bell 206B helicopter. The system is composed of cameras that measure the longitudinal tip-path-plane angle with respect to the fuselage and an air data boom fitted with a horizontal wind vane that measures the free-stream velocity in the longitudinal plane with respect to the fuselage. A global positioning system and inertial mass unit were also included to compare the measurements of the imaging system with the theoretical longitudinal tip-path-plane for a given drag-to-weight ratio, flight path angle, and acceleration. In general, the longitudinal tip-path-plane angle measurements compare well with theory and prove highly repeatable for steady-state flight maneuvers for the Bell 206B helicopter.

AN IMAGE-BASED APPROACH FOR TRACKING

HELICOPTER LONGITUDINAL TIP-PATH-PLANE ANGLE

by

Richard Sickenberger

Thesis submitted to the Faculty of the Graduate school of the
University of Maryland, College Park in partial fulfillment
of the requirements for the degree of
Master of Science
2008

Advisory Committee:

Dr. Fredric Schmitz, Chair
Dr. James Bader
Dr. Alison Flatau

Dedication

To my family.

Acknowledgements

Table of Contents

List of Tables

List of Figures

Nomenclature

A	Rotor disk area, m^2
c_{tip}	Tip chord length, m
D_f	Fuselage drag, N
dm/dt	Mass flow rate through actuator disk, kg/s
dy	Blade length element, m
dV/dt	Magnitude of aircraft acceleration, m/s^2
f	1) Equivalent flat plate area, m^2 (section 2.3)
	2) Focal length, m (section 4.1.1)
g	Acceleration due to gravity, 9.81 m/s^2
H	Rotor drag, N
I_b	Blade mass moment of inertia, $kg*m^2$
k	Shutter overexposure factor
L	Lift per unit length of blade, N/m
m	1) Mass per unit length of blade, kg/m (section 2.1)
	2) Inflow mass, kg (section 2.2)
Q_{Source}	Integrated irradiance of the light source, W/m^2
Q_{Sun}	Integrated irradiance of the sun, W/m^2
q_{Source}	Irradiance of the light source as a function of wavelength, W/m^2-nm
q_{Sun}	Irradiance of the sun as a function of wavelength, W/m^2-nm
R	Rotor radius, m
T	Rotor thrust, N

t_c	Time that the camera shutter remains open, *s*
V	Voltage, *volts*
V_∞	Free-stream velocity, *m/s*
$\bar{V}_\infty$	Non-dimensional free-stream velocity, V_∞ / v_h
v_h	Hover induced velocity, *m/s*
v_i	Induced velocity, *m/s*
$\bar{v}_i$	Non-dimensional induced velocity, v_i / v_h
W	Helicopter weight, *N*
w	Slipstream velocity, *m/s*
α_{TPP}	Longitudinal angle of the tip-path-plane with respect to the free-stream velocity, *deg* or *rad*
α_0	Angle of the free-stream velocity in the longitudinal plane with respect to the fuselage reference axis, *deg* or *rad*
α_1	Longitudinal angle of the tip-path-plane with respect to the fuselage reference axis, *deg* or *rad*
α_A	Longitudinal flapping angle of the aft blade with respect to the fuselage reference axis, *deg* or *rad*
α_F	Longitudinal flapping angle of the forward blade with respect to the fuselage reference axis, *deg* or *rad*
β	Flap angle relative to the hub plane, *deg* or *rad*
β_0	Coning flap angle relative to the hub plane, *deg* or *rad*
β_{1c}	1st harmonic longitudinal flap amplitude relative to the hub plane, *deg* or

rad

β_{1s}	1st harmonic lateral flap amplitude relative to the hub plane, *deg* or *rad*
β_{nc}	nth harmonic longitudinal flap amplitude relative to the hub plane, *deg* or *rad*
β_{ns}	nth harmonic lateral flap amplitude relative to the hub plane, *deg* or *rad*
γ	Flight path angle, *deg* or *rad*
λ	Wavelength, *nm*
$\bar{\lambda}$	Non-dimensional inflow, $\bar{v}_i - \bar{V}_\infty \sin\alpha$
ρ	Density of air, *kg/m^3*
ρ_c	Spectral response of the camera as a function of wavelength, $0 < \rho_c < 1$
ρ_f	Spectral response of the filter as a function of wavelength, $0 < \rho_f < 1$
ψ	Azimuth angle, *deg* or *rad*
Ω	Rotor angular velocity, *deg/s* or *rad/s*
(˙)	Time derivative, *d/dt*
(¨)	Double time derivative, *d^2/dt^2*
(*)	Azimuth derivative, *d/dψ*
(**)	Double azimuth derivative, *d^2/dψ^2*

Acronyms, Abbreviations, and Units

Bell 206B	Bell Helicopter, *"Jet-Ranger"*
BVI	Blade Vortex Interaction

CCTV	Closed Circuit Television
CVS	Compact Vision System
deg	degrees
GPS	Global Positioning System
EGI	Embedded GPS/INS
HSI	High Speed Impulsive
Hz	hertz
INS	Inertial Navigation System
IR	Infrared
IRIG	Inter-Range Instrumentation Group
kg	kilogram
kHz	kilohertz
kts	knots
LCD	Liquid Crystal Display
MIR	Micropower Impulse Radar
m	meter
N	Newton
PPDG	Portable Precision Display Guidance
Q-SAM	Quasi-static Acoustic Mapping
rad	radians
RNM	Rotorcraft Noise Model
s	second
TPP	Tip-Path-Plane

TTL	Transistor/Transistor Logic
UV	Ultraviolet
VDC	Volts Direct Current
VIR	Visible Infrared
W	watt

Chapter 1: Introduction

This section will address the fundamental acoustic problem of blade-vortex interaction and setup the roadmap for the development of a tip-path-plane imaging system. Also described are previous blade-tracking systems and their limitations in predicting the inflow state of the main rotor.

1.1   Blade-Vortex Interaction Acoustic Problem

Four of the primary acoustic sources of main rotor noise include thickness, loading, high-speed impulsive (HSI), and blade-vortex interaction (BVI) noise[1] (see Figure 1.1). Thickness noise, the result of a finite thickness rotor blade displacing air, causes unsteady pressure waves to radiate to the far field near the plane of the rotor. Loading noise, the fluid reaction to the lifting blade, causes pressure waves to radiate primarily out of the plane of the rotor. High speed impulsive noise arises when the blade tips travel at high mach numbers and experience local transonic aerodynamic effects in the plane of the rotor. The last primary form of rotor noise, blade-vortex interaction, is the impulsive noise resulting from rapid pressure fluctuations as the blade passes near or through previously shed rotor vortices. This source acts primarily out of the plane of the rotor.
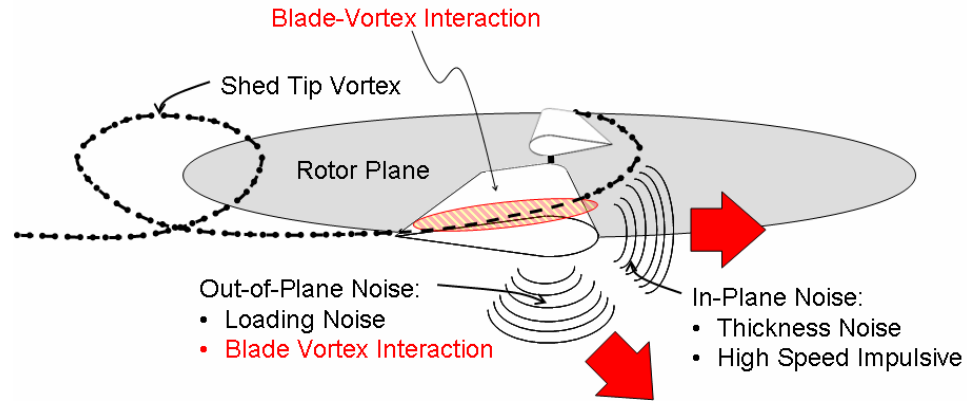
Figure 1.1: Four primary acoustic sources of a main rotor.

The intensity of BVI noise is dictated by the rotor's inflow[2]. In steady-state flight, the local inflow of the rotor influences the rotor wake position with respect to the blades (see Figure 1.2). This, in turn, determines the character and strength of the rotor noise that is emitted from the helicopter. When the rotor inflow is low and the blades pass close to previously shed tip vortices, large amounts of noise are emitted. When the magnitude of the rotor inflow is large, the blades pass farther away from the shed vortices and the radiated noise is much less. This is the fundamental principle on which the Quasi-Static Acoustic Mapping (Q-SAM)[3] approach is based. Implementation of Q-SAM has been made through theoretical modeling[3,4] and through measurement[5,6]. More recently, the theoretical and experimental implementation approaches are being integrated – creating the Rotorcraft Noise Model Q-SAM (RNM-QS) approach, which can also handle accelerating and decelerating flight in the longitudinal plane. It should be noted here that while inflow control can be used to mitigate the intensity of BVI noise, it cannot necessarily be used to change the intensity of the other aforementioned rotor acoustic sources.
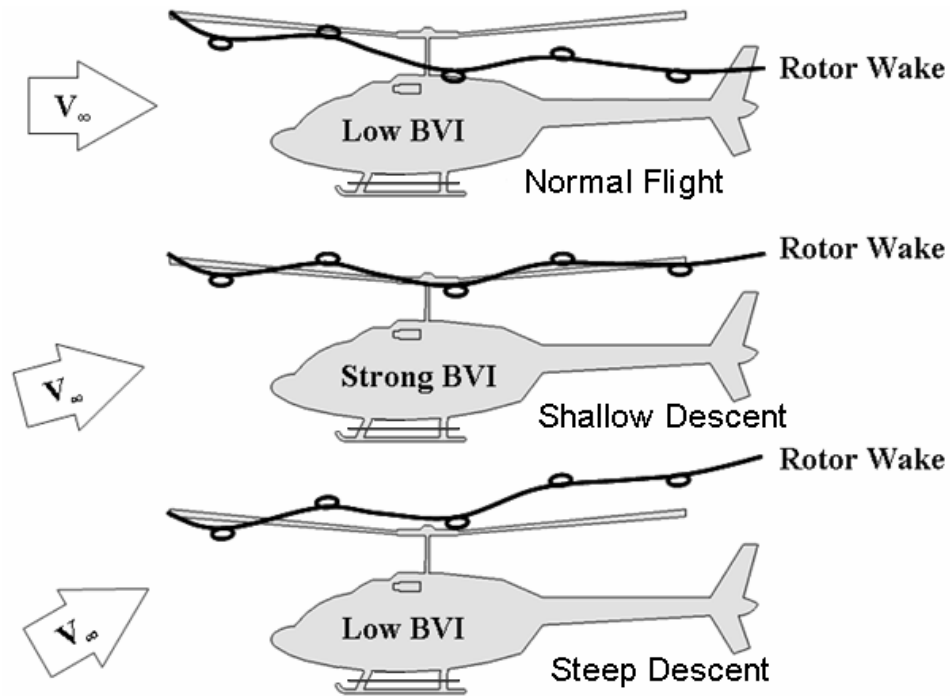
Figure 1.2: Relationship of inflow to BVI radiation in normal flight (top), shallow descent (middle), and steep descent (bottom).

As will be shown in Chapter 2, the inflow of the rotor is dependent on the longitudinal free-stream velocity and the longitudinal angle of the tip-path-plane – that is, the plane traced by the blade tips each revolution – with respect to the free-stream velocity. The longitudinal tip-path-plane angle can be visualized as a combination of two components: the longitudinal flapping of the rotor blades with respect to the hub plane and the angle of the hub with respect to the free-stream velocity. Here the hub plane refers to a plane orthogonal to the rotation of the rotor mast.

The first component, the flapping angle of the blades, is a combination of a steady-state coning angle caused by aerodynamic and centrifugal loads on the blade and an additional longitudinal flapping due to asymmetric loads on the rotor blades during forward flight (see Figure 1.3). The flapping angle is also composed of lateral and higher harmonic

3

flapping components. However, the lateral flapping component has no impact on the longitudinal position of the tip-path-plane and though the higher harmonic components do create some wobbling of the plane, they are negligible for a first order analysis[7].
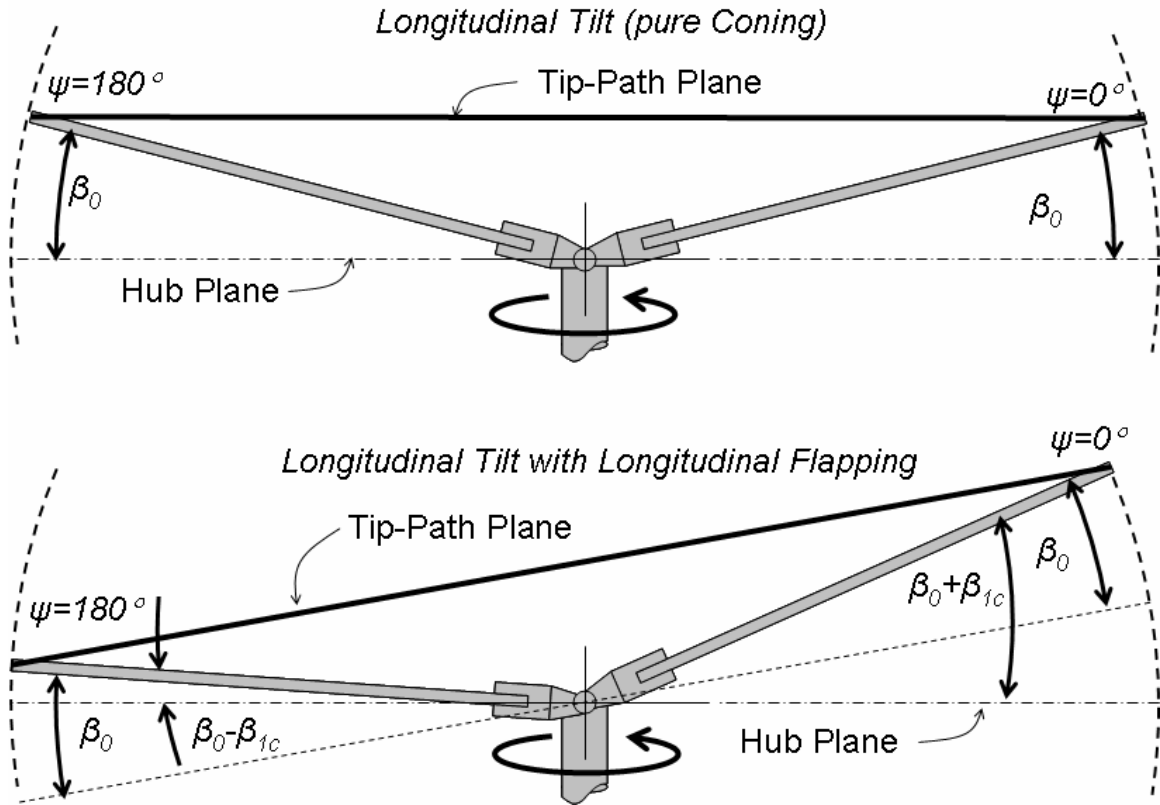
Figure 1.3: Longitudinal tilt for pure coning, β_0, (top) and with the longitudinal flapping component, β_{1c}, (bottom).

The second component, the angle of the hub plane with respect to the free-stream velocity, is a combination of the fuselage attitude with respect to the free-stream velocity and the rotor mast angle. Naturally, this description requires the center of gravity and trim tabs of the individual rotor blades be adjusted so that all blades are at the same effective position for a given azimuth angle in space.

1.2   Current Blade Tracking Systems

Current image-based blade tracking techniques generally fall into three categories: electro-optical tracking, strobe light tracking, and radar tracking[8]. Electro-optical systems are based on the contrast of the blades with respect to the background. Early systems, such as ground based tracking system developed by Chicago Aerial in the 1960s and the in-flight tracking system developed by Stewart Hughes in the 1980s, operated by monitoring changing lighting conditions as the blades passed over an optics assembly that focused light onto individual photo transistors[9]. Modern electro-optical concepts, developed by Helitune and Dynamic Solutions Systems, incorporate digital imaging techniques with line-scan cameras. Strobe light tracking systems, such as the 135M11 Strobex strobe, illuminate rotor tip targets with a strobe light triggered by each blade passing[10]. Generally these strobe-based systems require a trained observer to monitor blade alignment. Radar systems, such as the Micropower Impulse Radar (MIR), developed by the Lawrence Livermore National Laboratory for the V-22, provide digital images of a portion of the rotor blade[11]. Though radar systems are extremely accurate, they are also quite complicated and very expensive.

However, these systems, while an excellent starting point for a developing a tip-path-plane tracking system, have two fundamental limitations that prevents their use for BVI noise prediction and mitigation strategies. First, with the exception of the MIR system, they are only capable of providing the tip-path-plane angle at a single azimuth angle and cannot provide the longitudinal component of interest. Second, these systems are developed for blade tracking and balancing purposes to mitigate aeroelastic and

mechanical vibrations. These systems cannot be used to monitor the inflow state of the rotor since they do not reference the free-stream velocity. Therefore, these systems must be modified in order to obtain the desired information for BVI mitigation purposes.

Alternative means of tracking the rotor blade in the past include fitting teetering rotor systems with potentiometers and installing strain gages within the blades to measure deflection. However, these systems typically require alterations to the rotor blades and the installation of a slip ring.

This paper describes the design and evaluation of a system that is capable of tracking the plane of the rotor without requiring major alterations to the blade – so that when blades are changed or when the system is moved to a different helicopter, no major modifications are required. The system also must work in all types of lighting – including the out-of-doors, where sunrise and sunset present major obstacles to a robust design. An optics-based design for such a tracking system will be discussed in Chapters 3 and 4.

Chapter 2: Theory

This section will discuss the properties that govern the main rotor inflow. First, a general overview of blade flapping for a single rigid rotor will be addressed. Then, momentum theory will be used to derive the general inflow equation. The inflow equation will then be examined to identify the important variables. Lastly, a stead-state longitudinal force balance will be used to relate the longitudinal tip-path-plane angle to the drag-to-weight ratio, flight path angle, and acceleration of the aircraft.

2.1 Blade Flapping Equation Overview

Consider a rigid blade with a uniformly distributed mass rotating about an axis subject to aerodynamic loads. As shown in Figure 2.1, the mass element, *mdy*, is subject to three loads that create a bending moment about the flapping hinge. These loads include an aerodynamic, centrifugal, and inertial force.
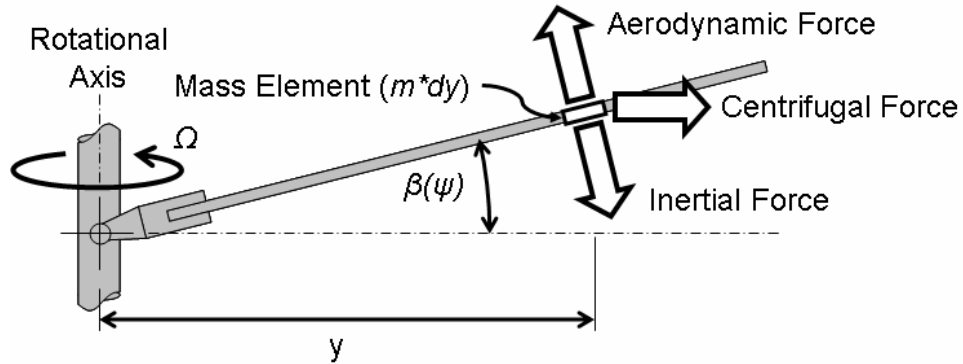
Figure 2.1: Flapping forces acting on a blade element.

If there is no hinge offset, the summation of the moments about the flap hinge for an articulated blade with small flapping angles yields:

$$\underbrace{\int_0^R my^2\Omega^2\beta\,dy}_{Centrifugal} + \underbrace{\int_0^R my^2\ddot{\beta}\,dy}_{Inertial} - \underbrace{\int_0^R Ly\,dy}_{Aerodynamic} = 0 \tag{2.1}$$

Where R is the blade radius, m is the blade mass per unit length, β is the flap angle, Ω is the angular velocity, and L is the lift per unit span of the rotor.

Recall that the mass moment of inertia is:

$$I_b = \int_0^R my^2 dy \qquad (2.2)$$

Collecting terms from the summation of mass moments yields:

$$I_b\ddot{\beta} + I_b\Omega^2\beta = \int_0^R Ly\,dy \qquad (2.3)$$

Recall that the azimuth angle, ψ, is the product of the constant rotational angular velocity and time. Therefore:

$$\dot{\beta} = \frac{d\beta}{dt} = \frac{d\beta}{d\psi}\frac{d\psi}{dt} = \Omega\frac{d\beta}{d\psi} = \Omega\overset{*}{\beta} \qquad (2.4)$$

And

$$\ddot{\beta} = \frac{d}{dt}\left(\dot{\beta}\right) = \frac{d}{d\psi}\frac{d\psi}{dt}\left(\Omega\frac{d\beta}{d\psi}\right) = \Omega^2\frac{d^2\beta}{d\psi^2} = \Omega^2\overset{**}{\beta} \qquad (2.5)$$

Therefore the time derivative equation can be rewritten in terms of the azimuth derivatives:

$$\overset{**}{\beta} + \beta = \frac{1}{I_b\Omega^2}\int_0^R Ly\,dy \qquad (2.6)$$

For forward flight, the general solution to the flapping equation can be represented as an infinite Fourier series of the form:

$$\beta(\psi) = \beta_0 + \sum_{n=1}^{\infty}\left(\beta_{nc}\cos n\psi + \beta_{ns}\sin n\psi\right) \qquad (2.7)$$

As mentioned previously, β_0 represents the constant coning angle of the blade relative to the hub plane and β_{nc} and β_{ns} represent the amplitude of the higher harmonic longitudinal

and lateral flapping components respectively. In the following momentum theory analysis, only the coning and first-harmonic components will be considered.

2.2　Derivation of the General Inflow Equation

To calculate inflow, it is necessary to derive the induced velocity. This can be done using momentum theory assuming the rotor to be an actuator disk with uniform inflow. Consider a helicopter in forward flight, represented in Figure 2.2.
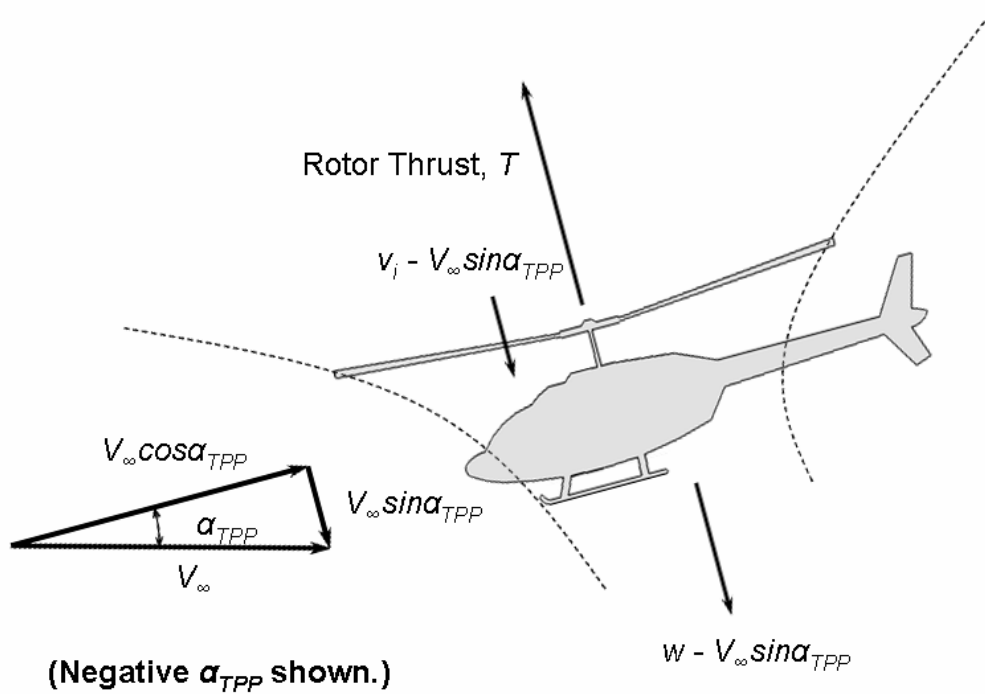
Figure 2.2: Momentum theory model for forward flight.

The mass flow rate influenced by the actuator disk, *dm/dt*, is a function of the fluid density, ρ, actuator disk area, A, and resultant velocity at the disk, U.

$$\frac{dm}{dt} = \rho A U \tag{2.8}$$

Here, the Glauert flow model is employed to represent the resultant velocity as a function of the free stream velocity, V_∞, the tip-path-plane angle, α_{TPP}, and the induced velocity in the plane of the rotor, v_i:

$$U = \sqrt{\left(V_\infty \cos\alpha_{TPP}\right)^2 + \left(v_i - V_\infty \sin\alpha_{TPP}\right)^2} \tag{2.9}$$

Applying the conservation of momentum yields thrust, T, in terms of the mass flow rate and the slipstream velocity, w:

$$T = \frac{dm}{dt}\left(w - V_\infty \sin\alpha_{TPP}\right) - \frac{dm}{dt}\left(-V_\infty \sin\alpha_{TPP}\right) = \frac{dm}{dt}w \tag{2.10}$$

Applying conservation of energy yields the rotor power, P:

$$\begin{aligned}
P &= T\left(v_i - V_\infty \sin\alpha_{TPP}\right) = \frac{1}{2}\frac{dm}{dt}\left(w - V_\infty \sin\alpha_{TPP}\right)^2 - \frac{1}{2}\frac{dm}{dt}\left(-V_\infty \sin\alpha_{TPP}\right)^2 \\
&= \frac{dm}{dt}w\left(\frac{w}{2} - V_\infty \sin\alpha_{TPP}\right)
\end{aligned} \tag{2.11}$$

Combining the two conservation equations simplifies to

$$2v_i = w \tag{2.12}$$

Therefore,

$$T = \frac{dm}{dt}w = 2\rho AUv_i = 2\rho Av_i\sqrt{\left(V_\infty \cos\alpha_{TPP}\right)^2 + \left(v_i - V_\infty \sin\alpha_{TPP}\right)^2} \tag{2.13}$$

Recall for hovering flight:

$$v_h = \sqrt{\frac{T}{2\rho A}} \tag{2.14}$$

Therefore, the equation for induced velocity becomes

$$v_i = \frac{v_h^2}{\sqrt{\left(V_\infty \cos\alpha_{TPP}\right)^2 + \left(v_i - V_\infty \sin\alpha_{TPP}\right)^2}} \tag{2.15}$$

Expanding the above expression generates the following quartic function

10

$$v_h^4 = v_i^4 + v_i^2 V_\infty^2 - 2v_i^3 V_\infty \sin \alpha_{TPP} \tag{2.16}$$

Introducing the non-dimensional parameters $\overline{v}_i = \dfrac{v_i}{v_h}$ and $\overline{V}_\infty = \dfrac{V_\infty}{v_h}$ yields

$$\overline{v}_i^4 + \overline{v}_i^2 \overline{V}_\infty^2 - 1 = 2\overline{v}_i^3 \overline{V}_\infty \sin \alpha_{TPP} \tag{2.17}$$

or

$$\overline{v}_i + \frac{\overline{V}_\infty^2}{\overline{v}_i} - \frac{1}{\overline{v}_i^3} = 2\overline{V}_\infty \sin \alpha_{TPP} \tag{2.18}$$

Consider the Taylor series expansion of the inflow equation non-dimensionalized with respect to the hover induced velocity

$$\overline{\lambda} = \overline{v}_i - \overline{V}_\infty \sin \alpha_{TPP} \approx \overline{v}_i \big|_{\alpha_{TPP}=0} + \alpha_{TPP} \frac{\partial \overline{v}_i}{\partial \alpha_{TPP}} \bigg|_{\alpha_{TPP}=0} - \overline{V}_\infty \alpha_{TPP} + H.O.T \tag{2.19}$$

The induced velocity at a zero tip-path-plane angle is found from the non-dimensional inflow expression:

$$\overline{v}_i^4 \big|_{\alpha_{TPP}=0} = \overline{v}_i^4 + \overline{v}_i^2 \overline{V}_\infty^2 - 1 = 0 \tag{2.20}$$

Therefore

$$\overline{v}_i \big|_{\alpha_{TPP}=0} = \sqrt{\frac{-\overline{V}_\infty^2 + \sqrt{\overline{V}_\infty^4 + 4}}{2}} \tag{2.21}$$

The differential term in the Taylor series expansion is found by differentiating the non-dimensional induced velocity function with respect to the tip-path-plane angle.

$$\left(1 - \frac{\overline{V}_\infty^2}{\overline{v}_i^2} + \frac{3}{\overline{v}_i^4}\right) d\overline{v}_i = \left(2\overline{V}_\infty \cos \alpha_{TPP}\right) d\alpha_{TPP} \tag{2.22}$$

Which simplifies to:

$$\frac{d\overline{v}_i}{d\alpha_{TPP}} = \frac{2\overline{v}_i^4 \overline{V}_\infty \cos \alpha_{TPP}}{\overline{v}_i^4 - \overline{v}_i^2 \overline{V}_\infty^2 + 3} \tag{2.23}$$

11

Evaluating the differential equation at a zero tip-path-plane angle yields

$$\frac{d\bar{v}_i}{d\alpha_{TPP}}\bigg|_{\alpha_{TPP}=0} = \frac{2\left(\bar{v}_i\big|_{\alpha_{TPP}=0}\right)^4 \bar{V}_\infty}{\left(\bar{v}_i\big|_{\alpha_{TPP}=0}\right)^4 - \left(\bar{v}_i\big|_{\alpha_{TPP}=0}\right)^2 \bar{V}_\infty^2 + 3} \tag{2.24}$$

Therefore, the inflow model from the Taylor series expansion becomes

$$\bar{\lambda} = \sqrt{\frac{-\bar{V}_\infty^2 + \sqrt{\bar{V}_\infty^4 + 4}}{2}} - \frac{2\bar{V}_\infty \alpha_{TPP}}{\bar{V}_\infty^4 - \bar{V}_\infty^2 \sqrt{\bar{V}_\infty^4 + 4} + 4} \tag{2.25}$$

If the product of the differential term and the tip-path-plane angle is small,

$$\bar{\lambda} \approx \sqrt{\frac{-\bar{V}_\infty^2 + \sqrt{\bar{V}_\infty^4 + 4}}{2}} - \bar{V}_\infty \alpha_{TPP} \tag{2.26}$$

Thus, the inflow for this model is related only to the free stream velocity and the tip-path-plane angle.

2.3 Longitudinal Force Balance

Next consider an estimation of the longitudinal tip-path-plane angle by referring to the longitudinal force balance diagram of the helicopter in a steady state condition:
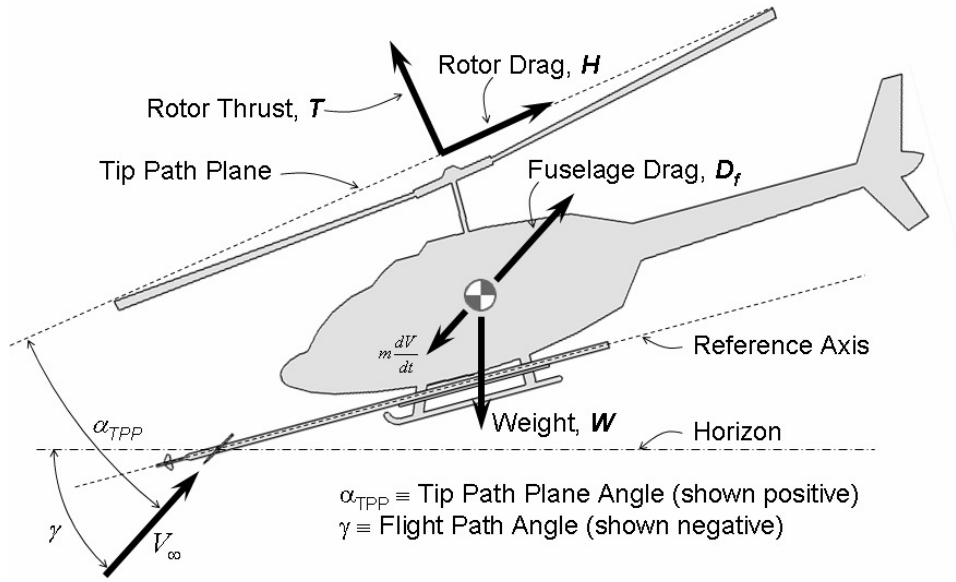
Figure 2.3: Longitudinal force balance diagram for steady state flight.

Taking the sum of the forces along the wind axis:

$$\sum \vec{F}_{V_\infty} = \frac{W}{g}\frac{dV}{dt} = -T\sin\alpha_{TPP} - H\cos\alpha_{TPP} - D_f + W\sin\left(-\gamma\right) \qquad (2.27)$$

Assuming small angles, and solving for the tip-path-plane angle yields

$$\alpha_{TPP} = -\left(\frac{D_f + H}{T} + \frac{W}{T}\gamma + \frac{1}{T}\frac{W}{g}\frac{dV}{dt}\right) \qquad (2.28)$$

Where the fuselage drag, D_f, is a function of the fluid density, equivalent flat plate area f, and free stream velocity:

$$D_f = \frac{1}{2}\rho f V_\infty^2 \qquad (2.29)$$

Assuming that thrust is equal to weight and that fuselage drag is much larger than the rotor drag, the theoretical tip-path-plane angle becomes:

$$\alpha_{TPP} \approx -\left(\frac{D_f}{W} + \gamma + \frac{1}{g}\frac{dV}{dt}\right) \qquad (2.30)$$

13

It should be noted that the theory defines the helicopter's tip-path-plane angle to be referenced to the undisturbed free-stream velocity of the helicopter. The next section will investigate two different approaches of measuring the tip-path-plane with respect to the free-stream velocity

Chapter 3: Measurement Technique

Measurement of the tip-path-plane with respect to the free-stream velocity is measured using a combination of two instruments: a wind vane or some other device that measures the angle of the free-stream velocity with respect to a fixed reference axis on the fuselage of the helicopter, α_0, and a camera system that measures the angle of the tip-path-plane with respect to the same reference axis, α_1. From geometry, the sum of the direct tip-path-plane measurement with respect to the helicopter fuselage line, α_0, and the angle of attack of the helicopter fuselage with respect to the free-stream velocity of the aircraft, α_1, yields the longitudinal tip-path-plane angle of the helicopter with respect to the free-stream velocity of the helicopter, α_{TPP} - the measurement that is directly related to BVI noise ($\alpha_{TPP} = \alpha_0 + \alpha_1$). This strategy is depicted in Figure 3.1.
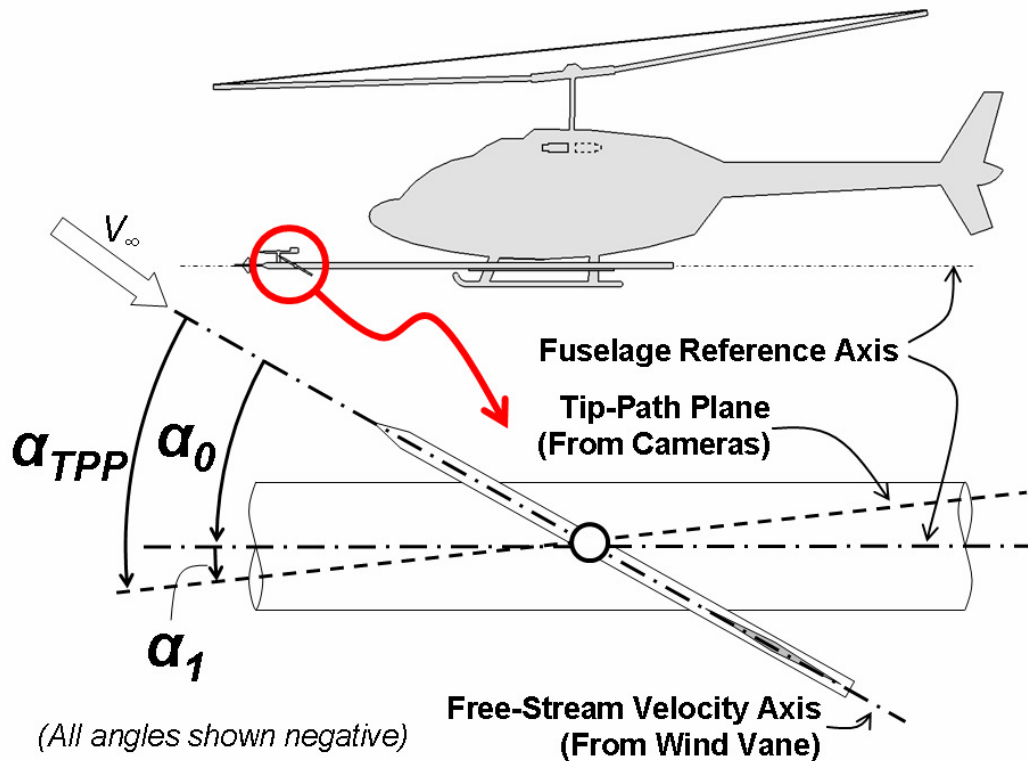
Figure 3.1: Measurement contributions for the longitudinal tip-path-plane angle.

In practice, there are really two ways of measuring the angle of attack of the helicopter reference line. The first is by employing a long measurement boom as shown in Figure 3.1. The second is to use an inertial measurement system to obtain the expected angle of attack based on the aircraft attitude and flight path.

3.1   Direct Measurement of α_0

The measurement of the free-stream velocity with respect to the reference axis is made using a swivel-head air data boom (Space Age Control model 100510). This data boom, shown in Figure 3.2, features sensors for recording total air pressure, static air pressure, angle of attack, and angle of slip.
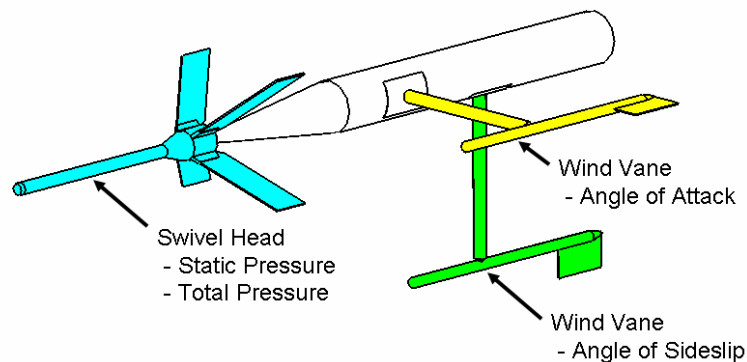
Figure 3.2: Diagram of Space Age Control 100510 Air Data Boom.

3.2   Indirect Measurement of α_0

An alternate method for measuring the angle of attack relative to the fuselage reference axis is to use an inertial measurement system. In this instance, the angle of attack relative to the fuselage can be found by referencing the inertial flight path angle of the helicopter and the attitude of the fuselage (see Figure 3.3). This approach has the advantage of not being susceptible to induced effects from the rotor, but requires the use of an inertial measurement system.
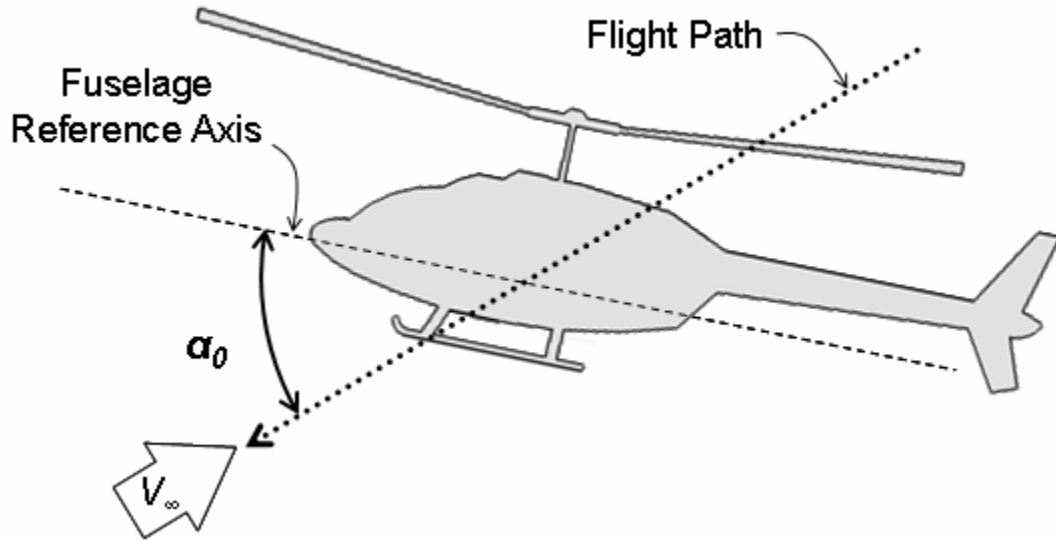
Figure 3.3: Alternate method of measuring fuselage angle of attack using an inertial system.

3.3 Measurement of α_1

The measurement of the tip-path-plane with respect to the reference axis can be found by using basic geometry (see Figure 3.4).
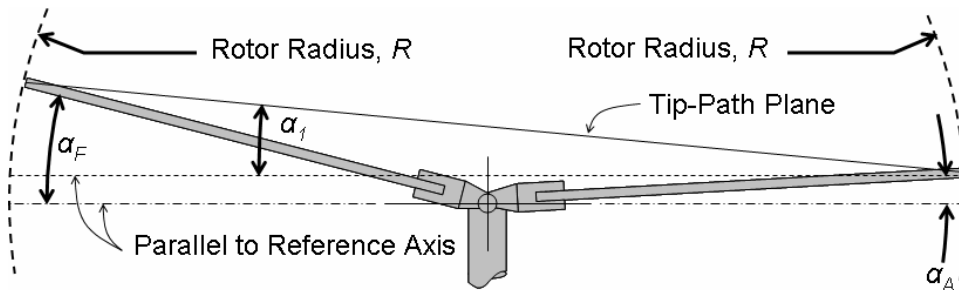
Figure 3.4: Main rotor blade flap geometry.

The tip-path-plane with respect to the reference axis, α_1, is calculated from the angles of the individual blades, α_F and α_A, with respect to the reference axis using basic trigonometric identities:

$$\alpha_1 = \arctan \frac{R \sin \alpha_F - R \sin \alpha_A}{R \cos \alpha_F + R \cos \alpha_A} = \arctan \frac{\sin \alpha_F - \sin \alpha_A}{\cos \alpha_F + \cos \alpha_A} \tag{3.1}$$

Recall the sum-to-product trigonometric identities:

$$\sin \alpha_F - \sin \alpha_A = 2\cos\left(\frac{\alpha_F + \alpha_A}{2}\right)\sin\left(\frac{\alpha_F - \alpha_A}{2}\right) \tag{3.2}$$

$$\cos \alpha_F + \cos \alpha_A = 2\cos\left(\frac{\alpha_F + \alpha_A}{2}\right)\cos\left(\frac{\alpha_F - \alpha_A}{2}\right) \tag{3.3}$$

Thus

$$\alpha_1 = \arctan \frac{2\cos\left(\dfrac{\alpha_F + \alpha_A}{2}\right)\sin\left(\dfrac{\alpha_F - \alpha_A}{2}\right)}{2\cos\left(\dfrac{\alpha_F + \alpha_A}{2}\right)\cos\left(\dfrac{\alpha_F - \alpha_A}{2}\right)} \tag{3.4}$$

Which simplifies to:

$$\alpha_1 = \frac{\alpha_F - \alpha_A}{2} \tag{3.5}$$

The final tip-path-plane angle, α, is then the sum of the two components, α_0 and α_1.

$$\alpha_{TPP} = \alpha_0 + \alpha_1 \tag{3.6}$$

Now, the task is to develop a system that can simultaneously capture the flap of the blades with respect to the reference axis to determine α_1. This was accomplished using cameras mounted to the fuselage that optically track the blade tips. The description of this system is provided in the next section.

Chapter 4: Equipment Setup

In flight data was recorded using three systems. Each system included a method for time synchronization using GPS time. Data recorded by the In-flight Data Recording System and the National Instruments Compact Vision System is used to calculate the tip-path-plane angle relative to the free-stream velocity using the measurement technique described in Chapter 3. Data recorded by the Portable Precision Display Guidance (PPDG) System is used to verify the tip-path-plane angle using the force balance approximation described in Chapter 2. A description of the relevant sensors recorded by each system is provided below.

Table 4.1: Equipment list.

System	Sensor	Measurement	Error
In-flight Data Recording System	Inter-Range Instrumentation Group (IRIG) Decoder	Time of day.	± 0.05 ms
	Space Age Control 100510 Air Data Boom	Angle of Attack relative to reference axis, α_0.	$\pm 0.5°$
		Free-stream velocity.	± 0.5 m/s
National Instruments Compact Vision System (CVS) 1450	Sony XCD-SX910 Monochrome Cameras	Angle of Tip-Path-Plane relative to reference axis, α_1.	$\pm 0.1°$
Portable Precision Display Guidance (PPDG) System	Ashtech Z-Sensor GPS receiver	Time of Day	± 0.05 s
	Honeywell H-764GU Embedded GPS/INS (EGI)	Velocity	± 0.1 m/s
		Acceleration	± 0.02 m/s^2
		Pitch Attitude	$\pm 0.05°$

These three systems are located on an equipment pallet installed in the cabin of a Bell 206B. This pallet also includes instrumentation for acoustics measurement experiments that were being conducted simultaneously with the tip-path-plane measurement.

Figure 4.1: Equipment pallet installed inside Bell 206 aircraft.

With the exception of the tip-path-plane imaging system, all of the sensors and recording equipment are commercial off the shelf components. The description of the tip-path-plane imaging system is provided below.

4.1 Longitudinal Tip-Path-Plane Imaging System Hardware

The longitudinal tip-path-plane imaging system is structured around the National Instruments Compact Vision System (CVS) 1450. Each blade revolution, a magnetic pick-up sensor (Shimpo model 3030AN) mounted on the main rotor shaft simultaneously triggers two Sony XCD-SX910 monochrome cameras – one pointed forward and the other pointed aft. A low power laser diode module mounted on each camera projects a beam through a concave lens and generates a vertical line in the same direction the cameras are pointed. Reflective targets mounted on the blade tips return a portion of this

vertical line to the cameras (see Figure 4.2). An interference filter matching the wavelength of the laser is installed on the camera to further improve the signal-to-background ratio. The captured images from both cameras are then passed to the CVS computer for image processing and longitudinal tip-path-plane angle calculation.
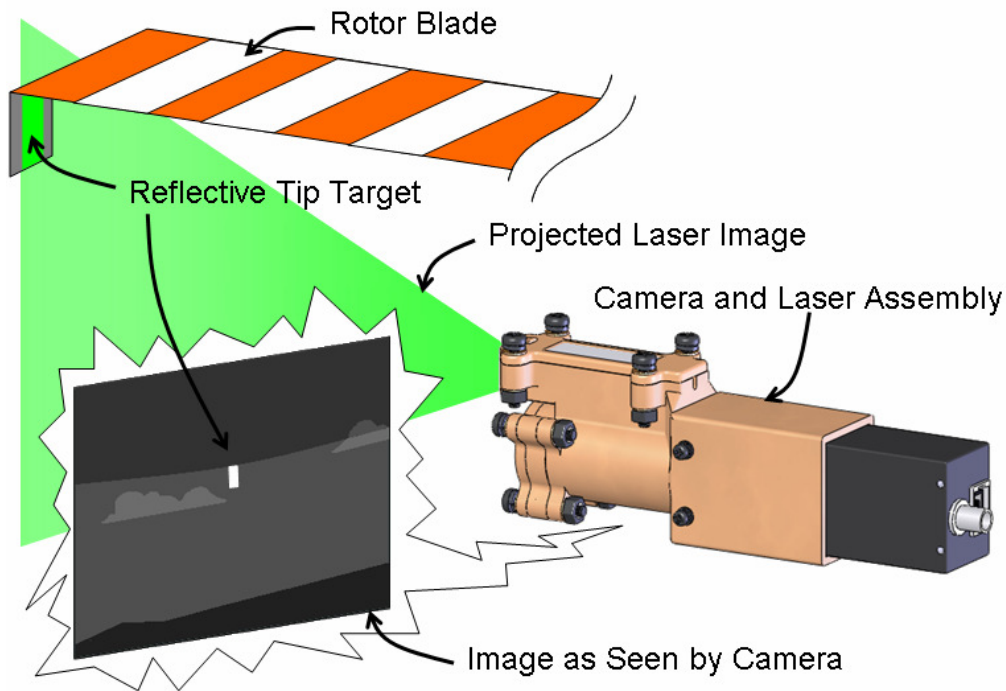
Figure 4.2: Overview of tip-path-plane imaging system.

4.1.1   Camera Assembly

To design the optics for the tip-path-plane tracking system, various light sources and optical filters were compared to optimize performance. Mathematical formulas for modeling filter transmission and filter performance due to source incidence angles were based on the methods presented in the Milles Griot[12] and CVI Laser[13] literature. Filter data including center wavelength, percent transmission, bandpass, optical density, and effective refractive index were provided by vendors including Milles Griot[12], CVI Laser[13], ThorLabs[14], Edmund Optics[15], and Omega Optical[16]. Laser module technical

21

data was provided by ThorLabs[14], US Lasers[17], Edmund Optics[15], and CrystaLaser[18]. Solar irradiance was modeled using the ASTM G173 standard for mean solar spectral irradiance at 37° latitude[19]. This standard represents the mean terrestrial solar irradiance within the continental United States.

Laser wavelength selection was made by considering the spectral response of the camera and the spectral makeup of the background light. The spectral response of the Sony XCD-SX910 and the ultra-violet light enhanced Sony XCD-SX910UV are shown below[20]. Notice that the peak spectral response of both cameras is near 532-nm - a common wavelength for solid-state commercial-off-the-shelf laser modules. Also notice that both cameras have diminished response in the infrared regions, and, while the XCD-SX910UV camera has a better response in the ultra-violet region than the XCD-SX910 model without the ultraviolet enhancement, response is still significantly lower than that for visible wavelengths.
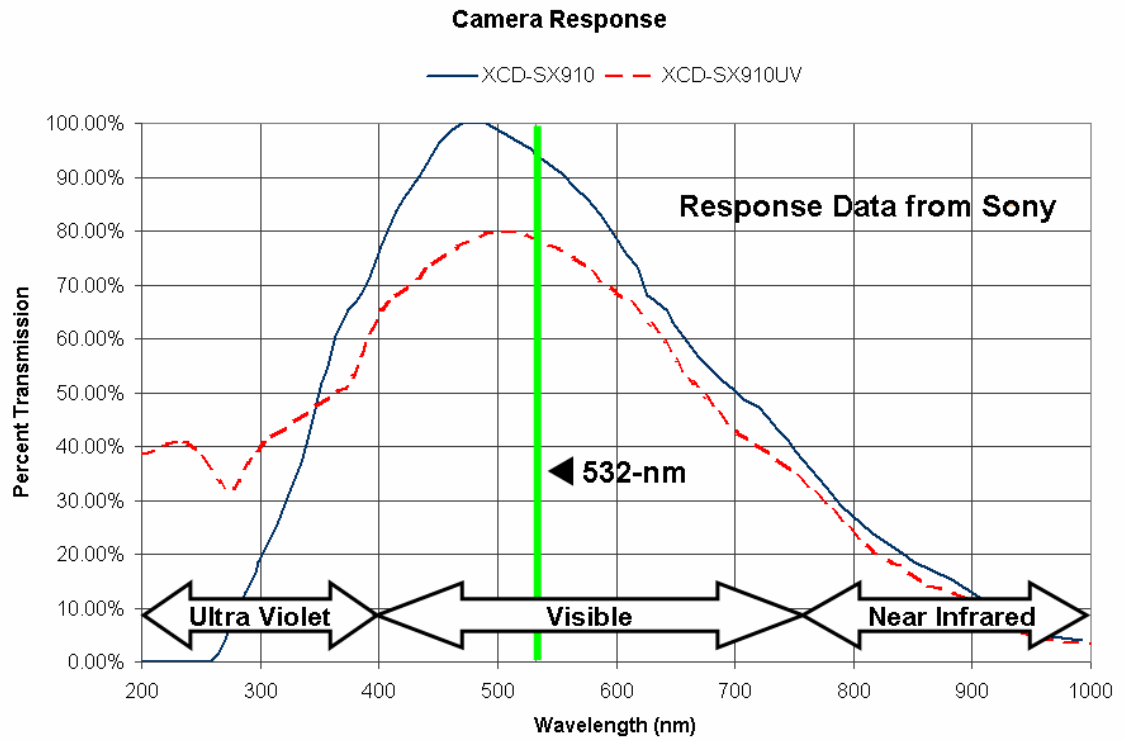
Figure 4.3: Spectral response of the Sony XCD-SX910 and XCD-SX910UV cameras.

The second consideration, the spectral makeup of the background, is best understood by referencing the mean solar irradiance for the continental United States. As shown in Figure 4.4, the wavelengths for the peak spectral response of the cameras coincide near the peak irradiance wavelengths for the sun. However, there are "dark" solar regions including UV wavelengths below 300-nm and wavelengths in the Visible-Infrared region around 760-nm and 950-nm where solar irradiance is quite low.
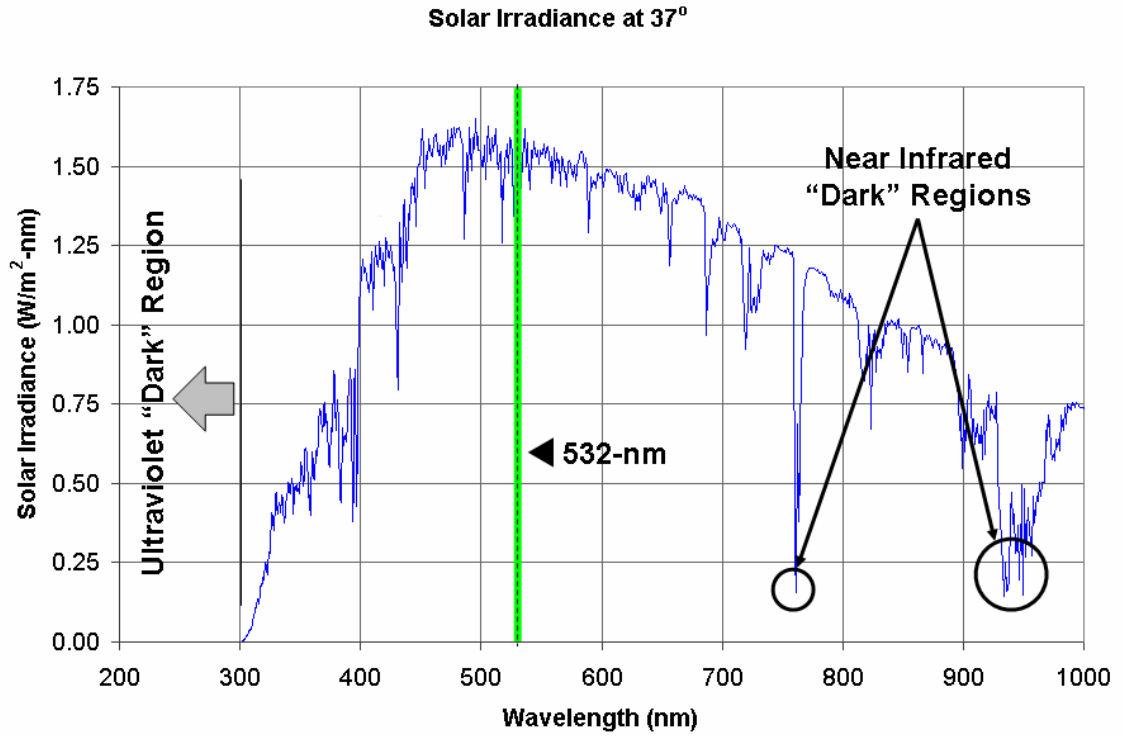
Figure 4.4: Mean solar irradiance for the continental United States.

Therefore, it is necessary to quantify the theoretical response of various source and interference filters by calculating the expected intensity of the source compared to the expected intensity of the background as seen by the camera. The source intensity, Q_{Source}, is found by integrating the product of the source irradiance, $q_{source}(\lambda)$, filter response, $\rho_f(\lambda)$, and camera response, $\rho_c(\lambda)$, over all wavelengths. Here $\rho_f(\lambda)$ and $\rho_c(\lambda)$ range from 0% to 100% transmission.

$$Q_{Source} = \int_0^\infty q_{Source}(\lambda) * \rho_f(\lambda) * \rho_c(\lambda) d\lambda \qquad (4.1)$$

The background intensity, Q_{Sun}, is found by integrating the product of the solar irradiance, $q_{sun}(\lambda)$, filter response, and camera response over all wavelengths. The response functions have the same meaning.

24

$$Q_{Sun} = \int_{0}^{\infty} q_{Sun}(\lambda) * \rho_f(\lambda) * \rho_c(\lambda) d\lambda \qquad (4.2)$$

The ratio of the source-to-sun intensity provides a theoretical metric for how visible the laser image would be if the camera were pointed directly at the sun. For example, a ratio of 50% would indicate that a pixel illuminated by just the laser would be half as bright as a pixel illuminated by the sun. The idea here is to select a source wavelength and an appropriate interference filter to make the laser stand out as much as possible when the image is acquired. That is, the ratio of source-to-sun intensity should be maximized.

The results of these calculations for several commercial-off-the-shelf laser and filter combinations are presented for the XCD-SX910 and XCD-SX910UV cameras in Table 4.2. The findings of this study suggest that using the green 532-nm laser with a 1.0-nm bandwidth is the best candidate. It should also be noted that while the theoretical gains of the XCD-SX910UV camera indicate superior performance to the XCD-SX910 camera, their expense does not warrant use for visible or near-infrared wavelengths. The purpose of considering the ultra-violet camera was to quantify any gains for using a 266-nm ultraviolet laser. However, this study indicates that using a wavelength in the "solar blind" region yields a theoretical source-to-background ratio below that of the sources studied in the visible and near infrared regions.

Table 4.2: Source to solar irradiance for various optics combinations.

λ_{source} (nm)	Bandwidth (nm)	Q_{Source}/Q_{Sun}	
		XCD-SX910	**XCD-SX910UV**
532	1	87.37%	104.66%
532	1.5	85.29%	85.17%
980	3.7	68.26%	80.79%
904	3	44.52%	44.79%
780	3	37.18%	37.39%

λ_{source} (nm)	Bandwidth (nm)	Q_{Source}/Q_{Sun}	
		XCD-SX910	XCD-SX910UV
532	2	30.89%	37.09%
650	3	32.83%	32.95%
635	3	31.81%	31.97%
532	3	30.05%	30.06%
904	10	17.28%	17.19%
266	10	0.81%	15.07%
980	10	15.04%	15.01%
850	10	12.94%	12.99%
808	10	12.55%	12.60%
780	10	10.92%	10.94%
660	10	9.46%	9.46%
650	10	9.33%	9.36%
640	10	8.92%	8.93%
532	10	8.46%	8.45%

An exploded view of the final camera assembly is shown in Figure 4.5. Additional components not mentioned previously include a circular polarizer to protect the optics from debris, a sun shield to shade the optics from reflections off of the fuselage, and a CCTV lens for focusing and controlling the amount of light that passes through the camera aperture.

1	Filter Assy Cap
2	Circ. Polarizer
3	Sun Shield Cone
4	Interference Filter
5	Concave Lens
6	Laser Module

7	Optics Housing
8	CCTV Lens
9	Camera
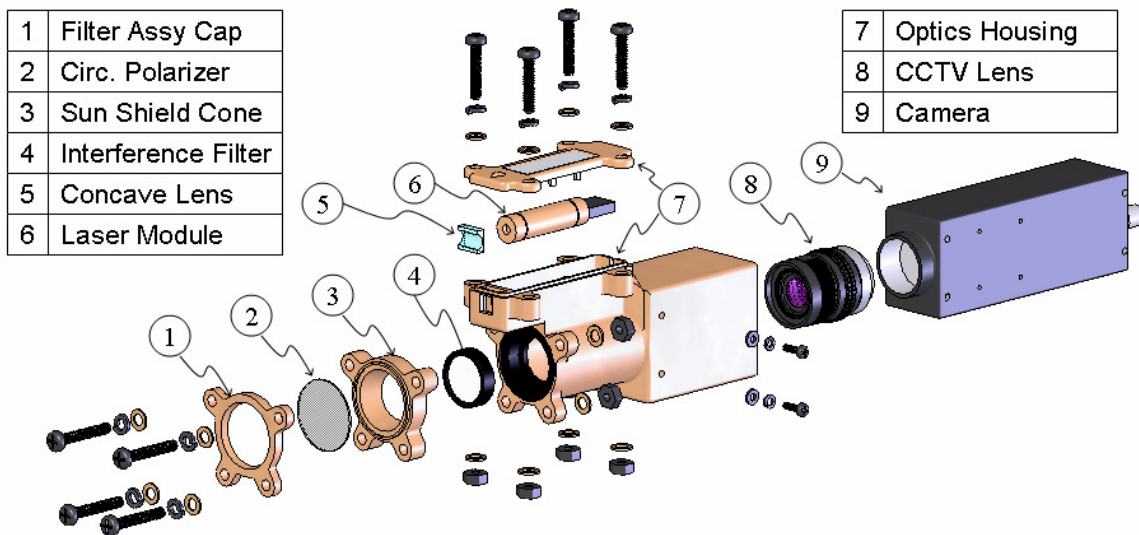
Figure 4.5: Exploded view of major components in the camera assembly.

The focal length of the concave lens is selected to match the expected range of flapping of the blades. If the focal length is too small, the area of the laser projection will be too large and the irradiance could be too low for detection. If the focal length is too large, the blade may flap outside of the range of the image.

During testing, the observed range of flapping for the Bell 206 fell within the projection angle of the concave lens. A histogram of the forward and aft blade positions is provided in Figure 4.6 for general flight both on and off steady-state conditions. As illustrated, the range of flapping seen by the forward camera is approximately 6.5° and the range of flapping seen by the aft camera is approximately 5°. Therefore, to generate the laser image, the camera system employed a concave lens with a focal length of 15 mm corresponding to an image that spread approximately 7.6° (see Figure 4.7).
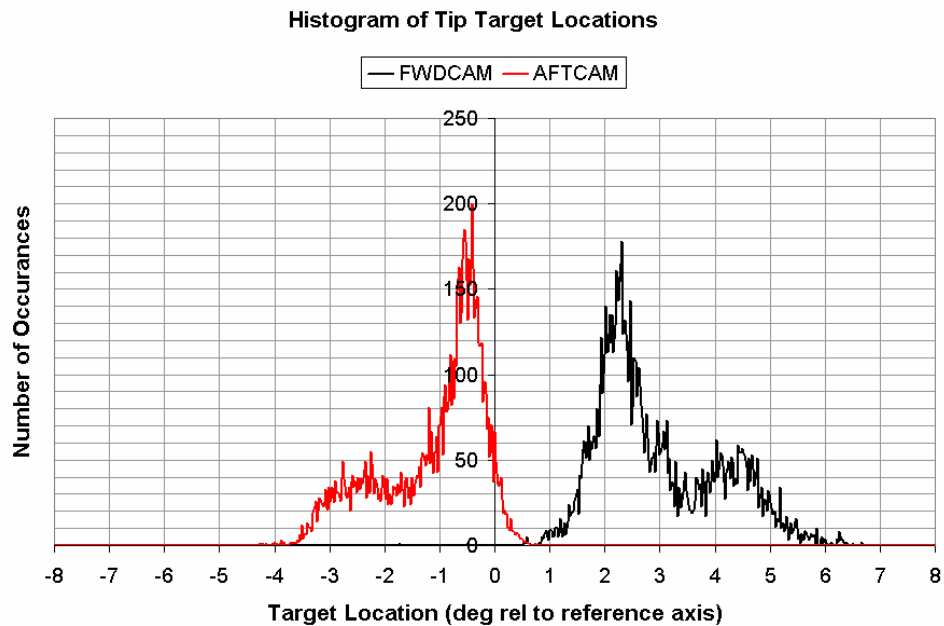
Figure 4.6: Statistical distribution of blade flap angles with respect to the reference axis.
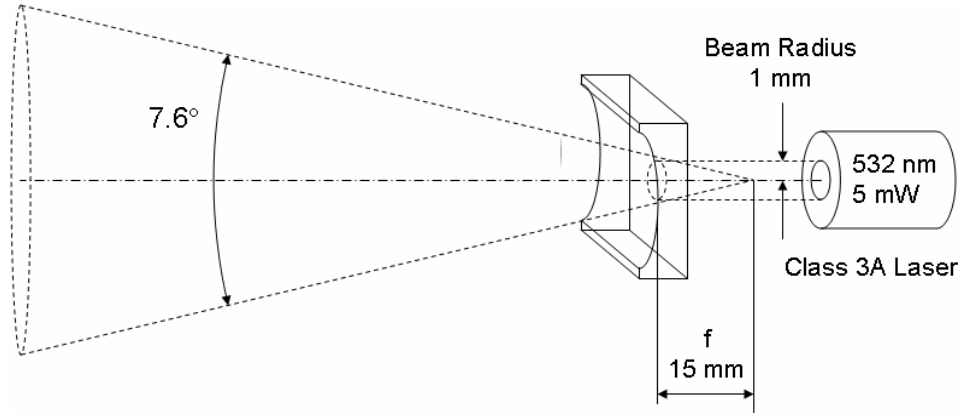
Figure 4.7: Concave lens optics geometry.

4.1.2 CVS Interface

The interface to the CVS-1450 computer is responsible for allocating power to the various components, conditioning the output of the one-per-rev sensor, triggering the individual cameras, sending synchronization data to the in-flight data recorder, and providing a status display for the user.
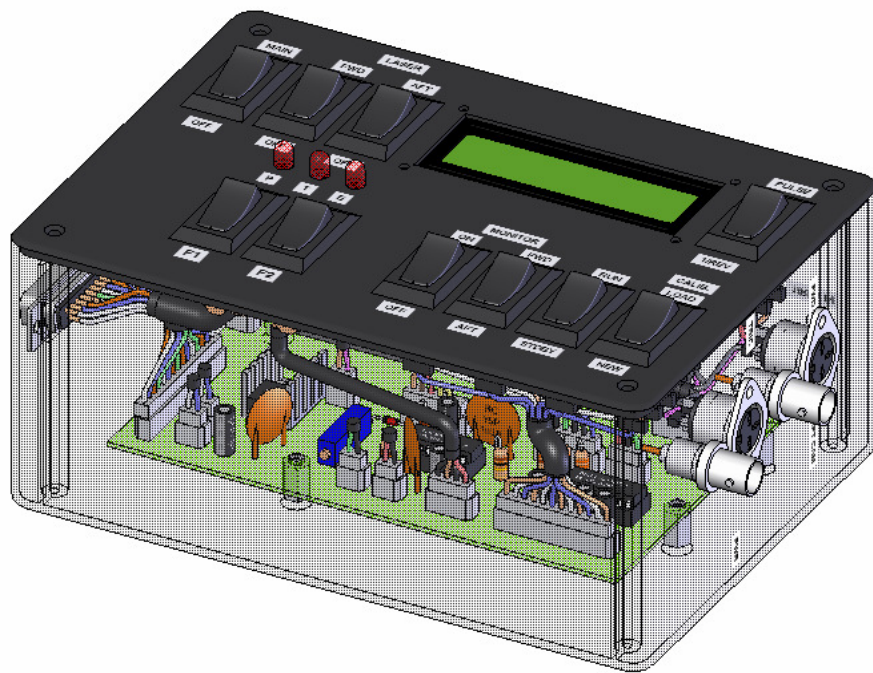
Figure 4.8: CVS Interface.

The first capability of the controller, power allocation, is provided so that the 24 VDC supply needed by the CVS-1450 computer and the 3VDC supply needed by the laser system can be interrupted at any time. The second capability of the controller, signal conditioning, transforms the analog signal from the one-per-rev sensor mounted on the main rotor shaft into a digital signal that triggers the embedded pulse generator of the CVS-1450 computer. This analog signal is first passed through an amplifier with variable gain and then through a bounceless switch. Once received by the CVS-1450, a pulse is returned to the controller and is then distributed to the cameras provided the controller is set to the recording mode. When the recording mode is selected, a logic signal is sent to the in-flight data recorder for post processing time synchronization. When the recording mode is deactivated, the logic signal returns to the base state. Lastly, the controller receives serial data from the CVS-1450 and passes it to an LCD display. This display typically indicates the recording mode, the calculated tip-path-plane angle, and any error messages.
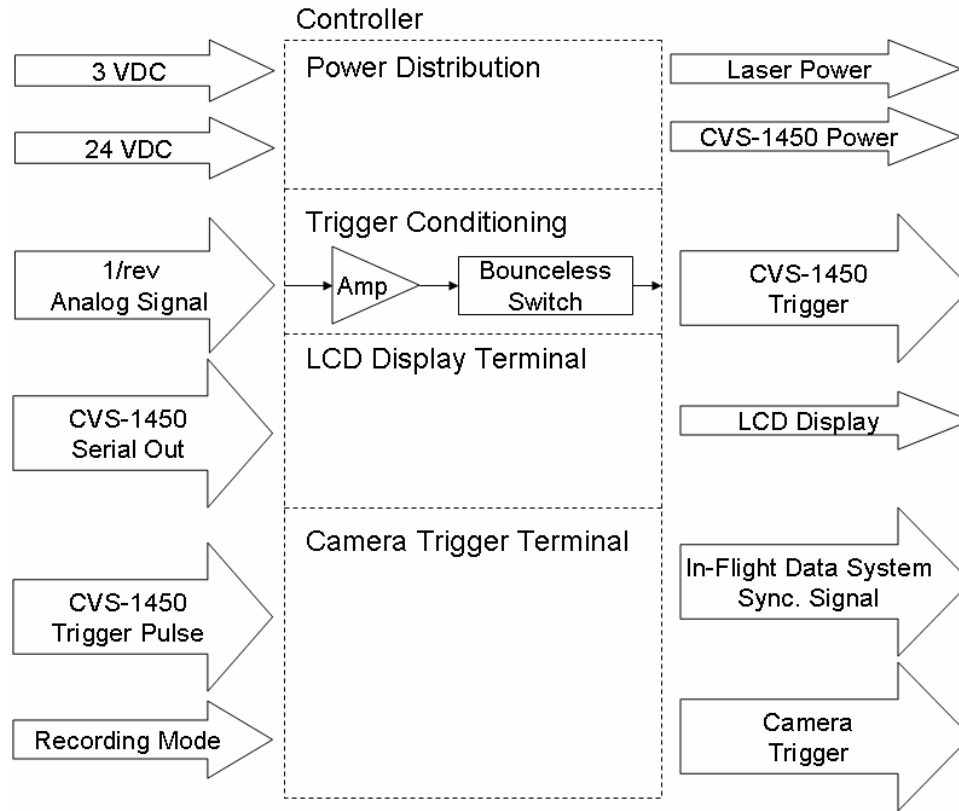
Figure 4.9: CVS interface operation diagram.

4.1.3 CVS-1450

The final component of the tip-path-plane imaging system, the CVS-1450, is the central processing unit for the system. This system provides a means of communicating with the individual cameras, pulse generation, image processing and data storage. All software for the CVS-1450 is written in the LabView environment.
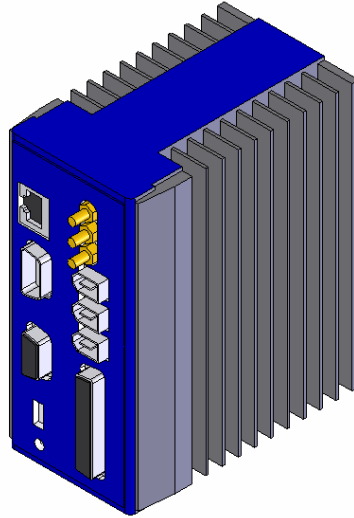
Figure 4.10: CVS-1450.

4.2 2006 Tip-Path-Plane Imaging System Software

The software installed on the CVS computer has two tasks. First, it takes the conditioned one-per-rev signal from the CVS controller and triggers the cameras once the blades have advanced into the camera field of view. Secondly, it takes the images returned by the cameras and attempts to locate the tip targets and calculate the relative angle of the tip-path-plane with respect to the fuselage. This section addresses each of these two routines.

4.2.1 Pulse Generation

The CVS-1450 has five output channels devoted to pulse generation using transistor/transistor logic (TTL) that are triggered by the conditioned one-per-rev signal. Upon triggering, the CVS-1450 sends a pulse to the cameras through the custom CVS interface. The shutters of the cameras remain open as long as the pulse logic remains high. Thus, the width of the pulse, t_c, is dictated by the angular velocity of the main rotor, Ω, rotor radius, R, and blade chord length, c_{tip}. A correction factor, k, is included to compensate for lead/lag effects and errors in camera positioning.

31

$$t_c = \frac{k * \tan^{-1}\left(\dfrac{c_{tip}}{R}\right)}{\Omega} \qquad (4.3)$$

4.2.2 Blade Tracking Algorithm

The tip tracking algorithm operates by comparing columns of pixels where the laser is known to be located with columns of pixels where the laser is known to be absent. The general philosophy of this algorithm is to remove as much of the background from the image as possible to isolate the illuminated tip target. This comparative approach also easily adapts to varying light conditions and is very inexpensive in terms of resources required for computation.

Consider the typical operation depicted in Figure 4.11. Since the camera, laser module, and all of the optics are rigidly fixed together, the reflection of the vertically projected laser line will always appear in the same column of pixels of the image acquired by the camera. This is indicated by the column with the white arrow in Figure 4.11. By the same reasoning, the remaining columns of pixel in the image are guaranteed to *not* contain the reflection. Background columns are indicated by the columns with black arrows in Figure 4.11. If the source column and the background column are reasonably close, they should, in theory, contain similar artifacts with the exception of the illuminated tip target. The difference of the two should be the isolated tip target.
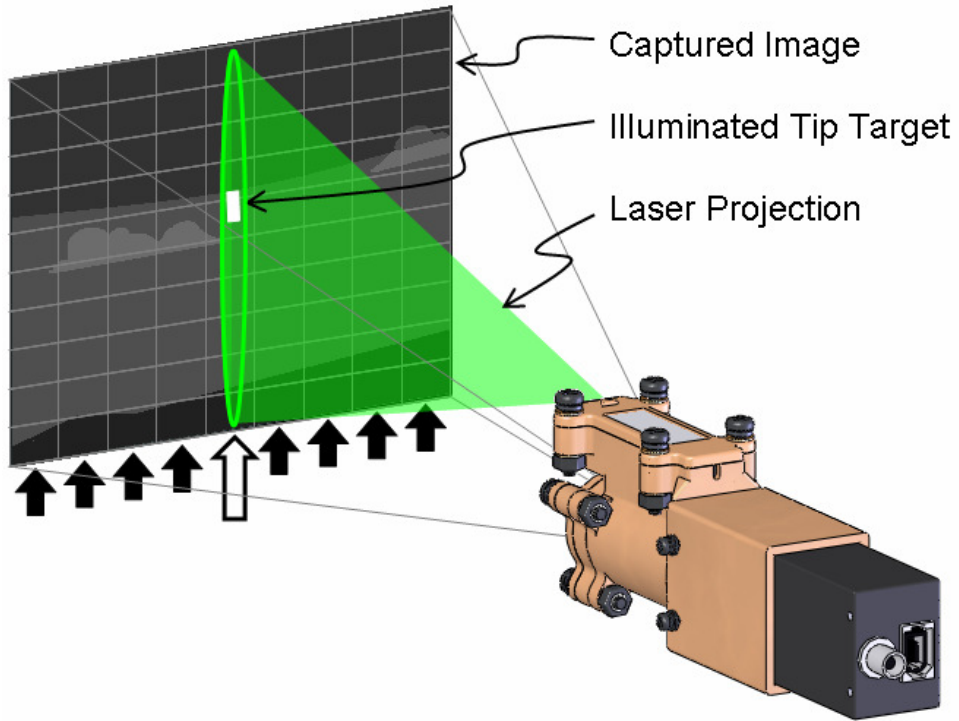
Figure 4.11: Generalized image acquisition scenario.

In practice, four columns are used for background information – two to the left of the laser image and two to the right of the laser image. This is to compensate for stray artifacts from ground objects that may only exist in a single column. The mean of the grayscale values for each row of these four columns of background data is then subtracted from each row of the column that contains the laser image. A typical image is presented in Figure 4.12. Note that at the location of the tip target the column containing the laser image (Interrogation Line 3) clearly stands out over the background.
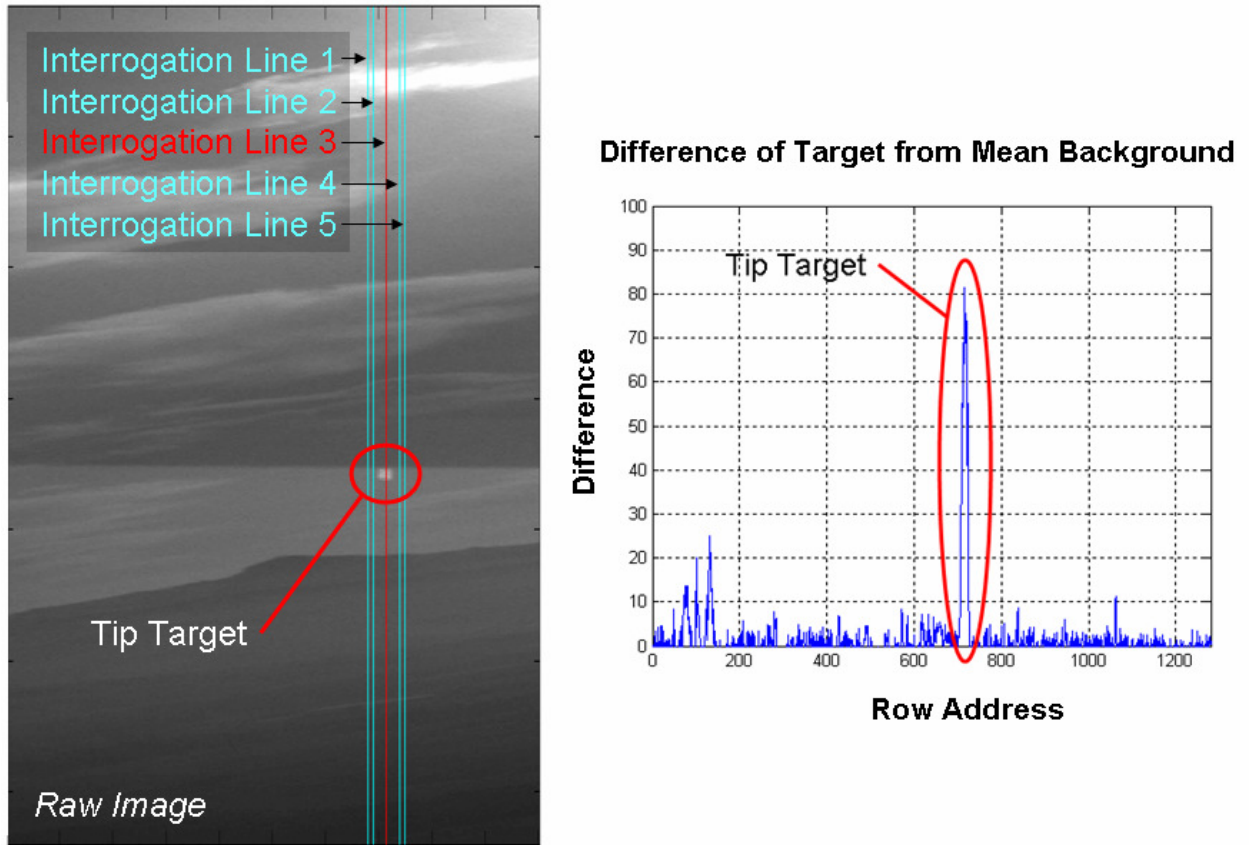
Figure 4.12: Example of image cross section data.

Another feature of the algorithm is its ability to adjust the region of interest for processing. That is, once the camera has identified the tip target, the algorithm only applies the differencing routine to rows of data immediately above and below where the target was previously located. This window is reduced only to a limit so that a sudden blade movement would not push the target out of the frame. If the target is not located, the algorithm executes a searching procedure to attempt to relocate the target.

A series of still images during turning flight is shown in Figure 4.13. The computed location of the tip target is indicated by the green circle and the region of interest is indicated by the blue box. In the first two frames, the region of interest is already reduced

34

to the limit and the indicator shows that the tip target is identified. As the sun passes through the image over the next four frames, the image becomes saturated by light and the tip target is lost. During this time, the region of interest expands. In the second-to-last image, the sun begins to exit the frame and the tip target is again located. The region of interest begins to contract in the final frame.

In each frame of Figure 4.13, the number at the top of the image is the mean grayscale value of the region of interest. The approximate incidence angle between the camera and the sun is indicated at the bottom of each frame.
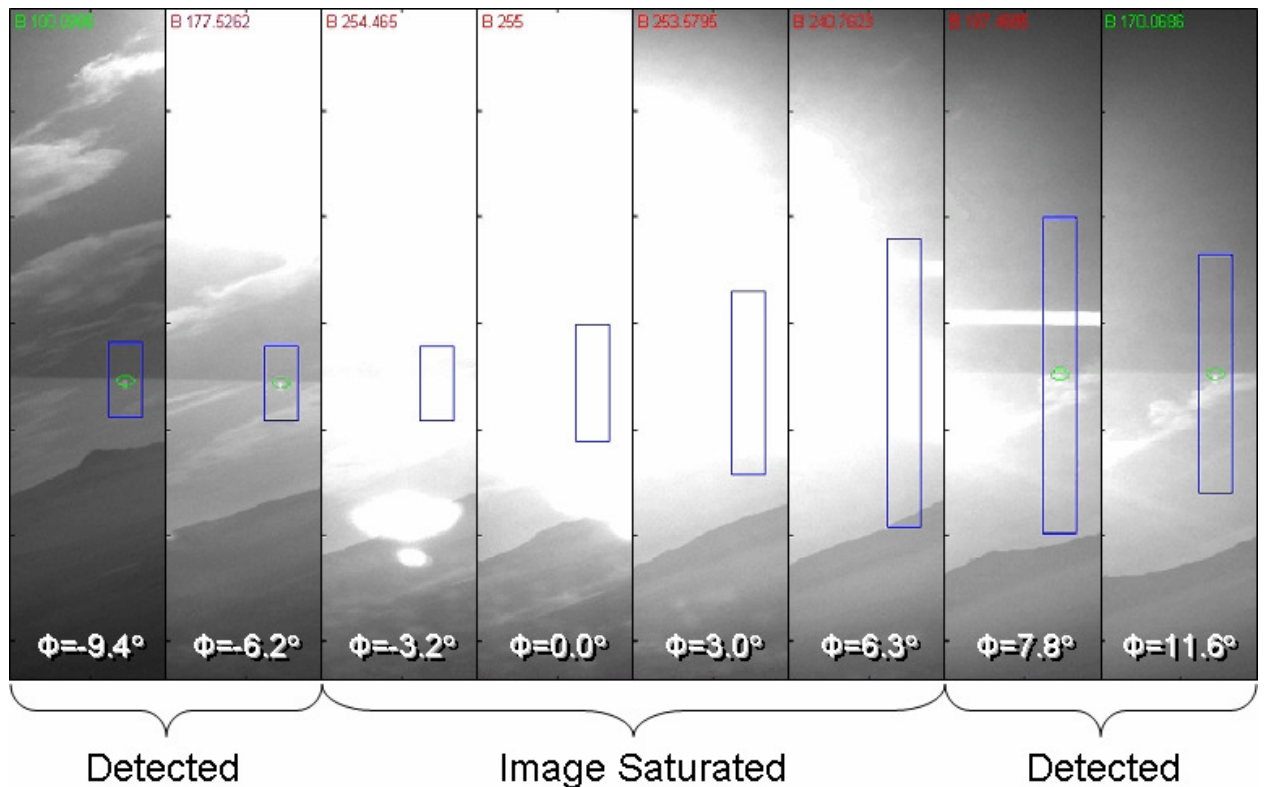
Figure 4.13: Tracking algorithm during a turning maneuver.

4.3   Equipment Installation

Figure 4.14 shows the general layout of the external equipment used by the longitudinal tip-path-plane measurement system. The air data boom is attached to the step on the port landing skid and each camera assembly is attached to the fuselage via maintenance hand grips near the engine cowling. The tip-targets used on the main rotor blades are the same targets used for track and balance systems, but they have been covered with a piece of retro-reflective tape. The inertial measurement system used by the PPDG is located inside the cabin.
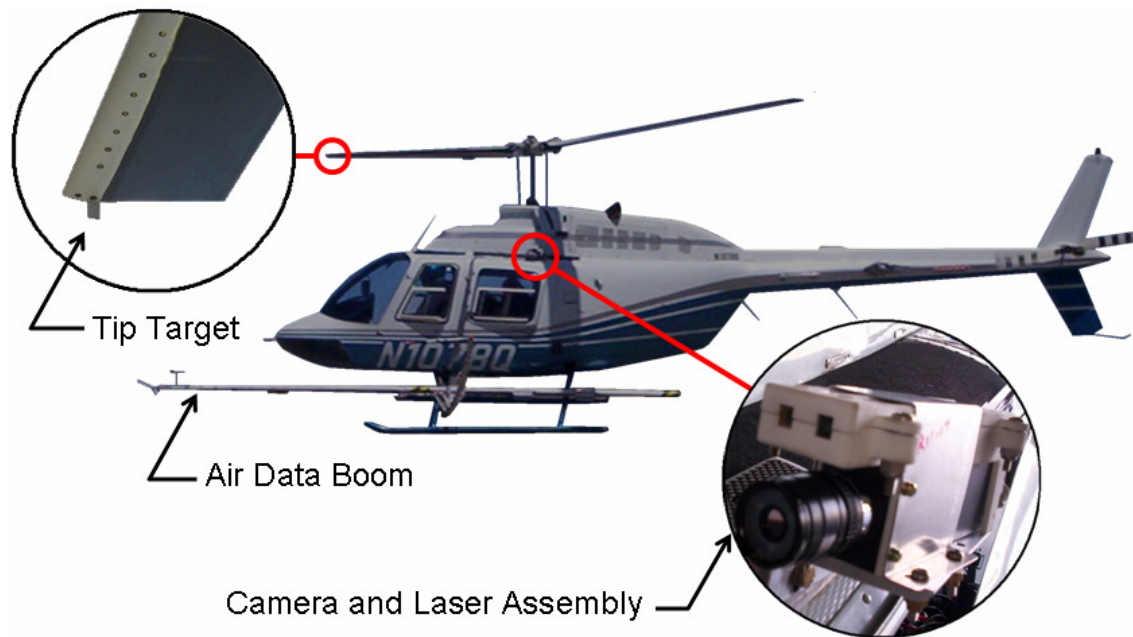
Figure 4.14: Bell 206 with external equipment installed.

Chapter 5: Testing Procedure

In June 2006, the aforementioned tip-path-plane imaging system was demonstrated at the NASA Ames Research Center at Moffet Field, California. In June 2007, a similar test was conducted at Gilroy, California. The purpose of these tests was to evaluate the performance of the system and verify the first-order relationships mentioned earlier.

5.1   Calibration

The following section describes the calibration process for the wind-vane on the air data boom and the blade tracking system.

5.1.1   Air Data Boom Calibration

The first part of the alpha vane indicator calibration is done by using a vane calibration fixture supplied by SpaceAge Control on the ground. With the indicator attached to the air data boom, the vane is positioned to various angles and the output voltage of the sensor read by the in-flight data recorder. The first part of the calibration process determines the linear relationship between the output voltage and the vane angle. This data is shown in the figure below.
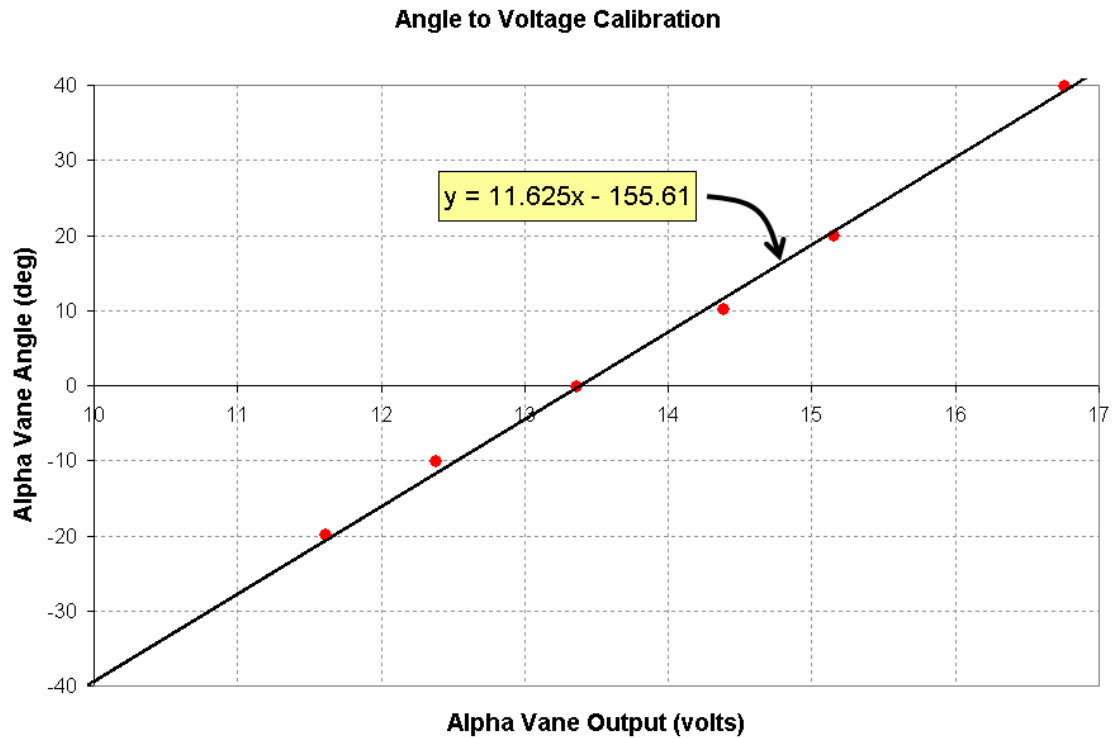
Figure 5.1: Alpha vane ground calibration.

An additional step is required in calibrating the alpha vane sensor to adjust for in-flight conditions. Consider the level flight scenario illustrated in Figure 5.2. In the top frame, the boom is infinitely far from the helicopter. In this situation, if the boom is pitched to some angle, θ, the angle of attack, α, of the vane with respect to the free-stream velocity should match the pitch angle. However, since the air data boom is a finite distance from the rotor, the induced velocity of the rotor along with other effects result in an angle of attack measurement different from the pitch angle. This error will naturally be a function of the airspeed of the helicopter.
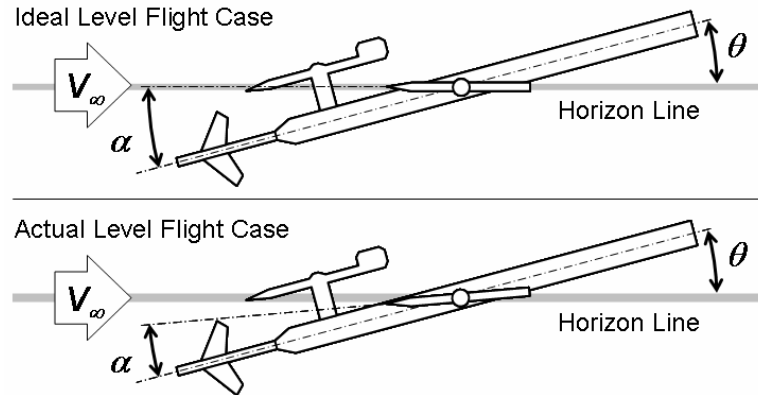
Figure 5.2: Ideal (top) and actual (bottom) alpha vane deflections for identical flight conditions.

To quantify this error, the aircraft was flown in level flight at various velocities. The difference between the angle of attack and the pitching attitude of the helicopter was found by comparing the output of the alpha vane indicator to the pitch angle recorded by the Portable Precision Display Guidance system. The results of this calibration run are provided below. In this plot, the abscissa axis represents the angle-of-attack reported by the air data boom and the ordinate axis represents the pitching attitude reported by the inertial system.
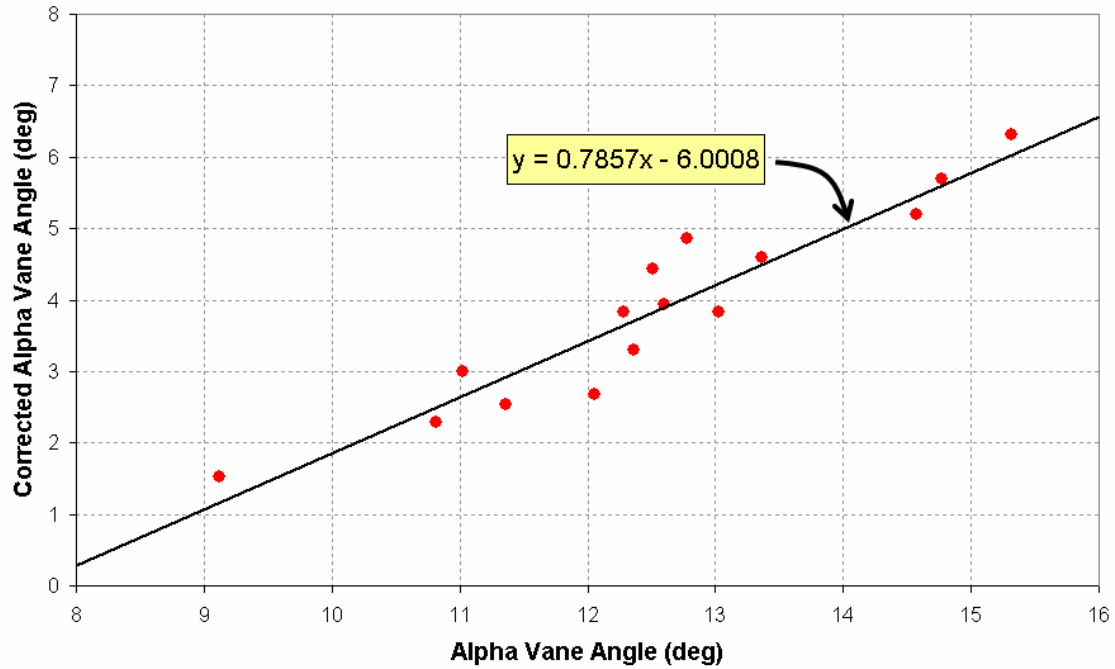
Figure 5.3: Alpha vane angle correction.

Combining the two calibration procedures yields the relationship between the angle of attack relative to the reference axis with the induced effects removed, α_0, and the voltage output from the alpha vane sensor, V:

$$\alpha_0 = 9.135V - 128.278 \tag{5.1}$$

In the above expression, the angle is reported in degrees.

5.1.2   Tip-Path-Plane Imaging System Calibration

To calibrate the imaging system, the blades were manually placed at known angles relative to the reference axis and still images were recorded by the CVS computer. The tracking algorithm was applied to these stills to identify the vertical pixel address corresponding to the blade tip (see Figure 5.4).   These data are used to provide the

individual blade flapping angle as a function of the vertical pixel address. A typical

relationship is shown in Figure 5.5.
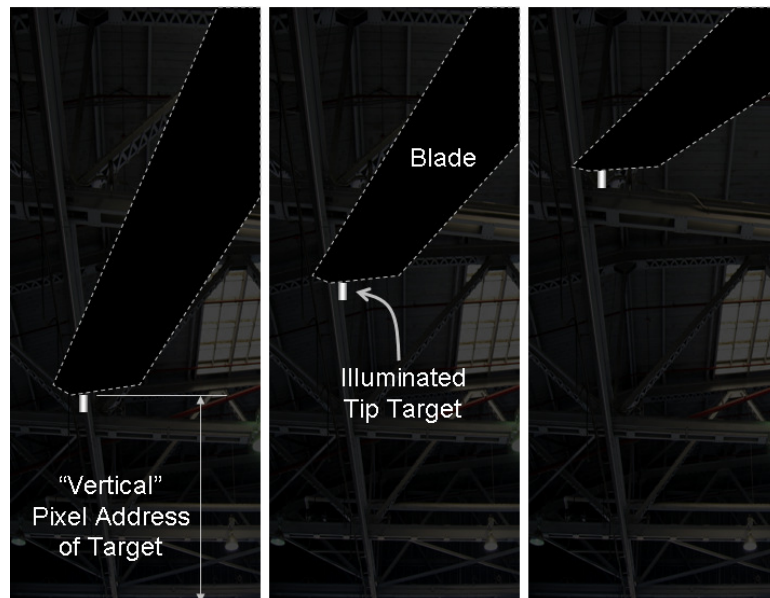
Figure 5.4: Sample still images for blade position calibration. Blade location highlighted.

Typical Calibration of Angle to Pixel Address

$y = -0.0228x + 11.92$
$R^2 = 0.9976$
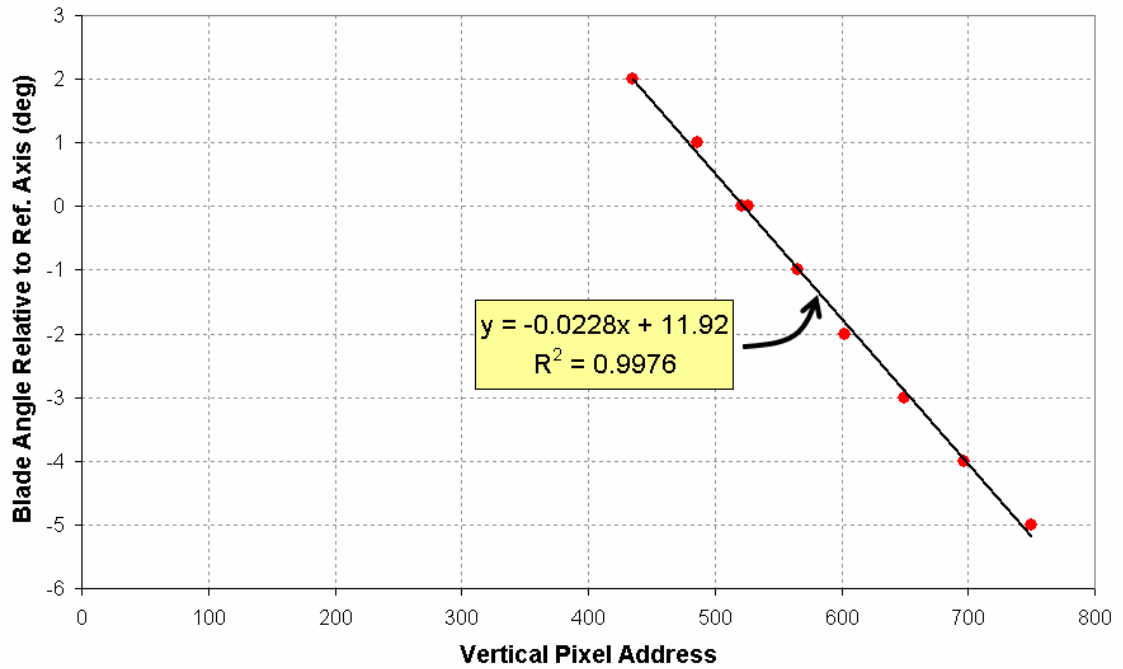
Figure 5.5: Typical example of camera calibration.

5.2 Flight Maneuvers

Because the governing equations that are used to quantify the tip-path-plane angle assume a steady maneuver, NASA's Pursuit Precision Display Guidance (PPDG) system was installed in the Bell 206 aircraft. This guidance system provided a display with piloting cues to maintain a given flight condition (see Figure 5.6). These maneuvers included level flight, ascents and descents, accelerations and decelerations, and various turns.

Figure 5.6: PPDG display mounted in cockpit.

The following maneuvers were used to validate the performance of the tip-path-plane imaging system.

Table 5.1: Flight maneuvers.

Run Number	V (kts)	Flight Path Angle, γ (deg)	Run Number	V (kts)	Flight Path Angle, γ (deg)
13/78	60	0	14/97	50	0
13/79	70	0	14/98	50	0
13/80	50	0	14/100	60	0
13/81	60	-3	14/101	60	0
13/82	60	-6	14/102	70	0
13/83	60	-7.5	14/103	70	0
13/85	60	-9	14/104	65	0
13/86	60	-10.5	14/105	65	0
13/87	60	-9	14/106	55	0
13/88	60	-12	14/107	55	0
13/89	60	-13.5	14/108	45	0
13/90	60	-15	14/109	45	0
13/91	70	-3	14/110	40	0
13/92	70	-6	14/111	40	0

Run Number	V (kts)	Flight Path Angle, γ (deg)	Run Number	V (kts)	Flight Path Angle, γ (deg)
13/93	70	-9	14/112	75	0
			14/113	75	0

5.3   Data Recording Process

The various phases of a maneuver are shown in Figure 5.7. The maneuver first starts with a basic pattern flight. Upon entering the final leg of the pattern, the pilot, under the guidance of the PPDG system, enters a level flight condition identified as the "Setup" portion of the flight path. Once the steady state condition has been reached, the pilot enters the desired maneuver. This can include any combination of velocities, accelerations, flight path angles, and turns. During this phase, the PPDG system provides the pilot cues necessary to maintain the flight condition of interest. This section of the maneuver, labeled "Recording Region" in the figure, is also the region where data is collected from the various systems. At the end of the recording region, the data recording devices are deactivated and the pilot reenters the basic flight pattern.
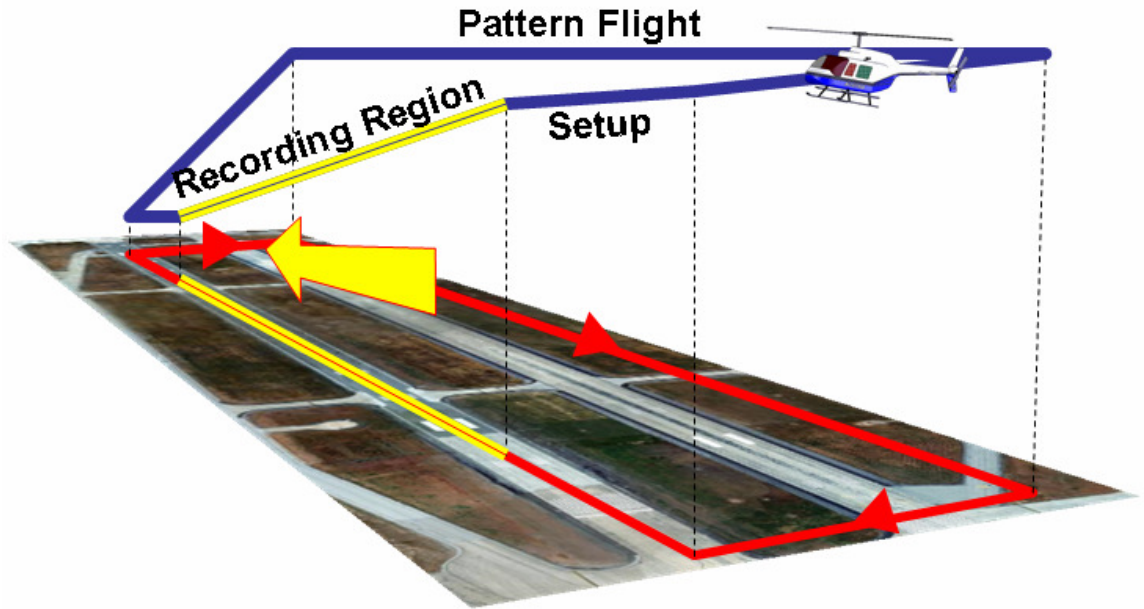
Figure 5.7: General layout for flight maneuver. The ground track is shown in red. The region of data record is highlighted in yellow.

5.4   Data Synchronization

Since each of the three primary systems (In-flight Data Recording System, Compact Vision System, and Portable Precision Display Guidance) each had their own clocks, attention should also be drawn to the process used to synchronize the data. The In-flight and PPDG system both included instruments that could record time from global positioning systems. Therefore, each data record contained a universal time stamp accurate to the sampling rate of the system – 50 µs for the in-flight data recorder and 1 ms for the PPDG system.

However, the CVS system did not include a clock. Instead, when the data was logged using the CVS system, a logic signal was sent to one of the channels of the in-flight data recorder. At the end of the maneuver, the CVS system was switched to a stand-by mode

and a second logic signal was sent to the in-flight data recorder. Once the CVS system had entered the stand-by state, the recording process for the other two systems was terminated. Since the in-flight system recorded the output of the one-per-rev sensor and the CVS processed an image each revolution, once the one-per-rev markers on the in-flight data were matched with the global positioning system time, the tip-path-plane imaging system data could also be synchronized.

Chapter 6: Results

The following section describes the results collected from the California flight tests on the Bell 206B.

6.1   Data Reduction Strategy

As mentioned previously, the first step in the data reduction process was to synchronize all of the data records using the onboard global positioning system clocks and the one-per-rev signal from the magnetic pick-up. However, each instrument suite recorded data at different sample rates. For instance, the in-flight data recording system typically recorded at 20 kHz, the PPDG at 1 kHz, and the CVS system once per revolution – or approximately 6.5 Hz.

To map all of the data to a common time scale, the data was first passed through a 1 Hz averaging window to remove all high frequency noise in the data. Though the assumptions made in the preceding derivations assume a steady-state flight condition, small transients in the flight condition were unavoidable and the averaging window removed many of the unsteady effects. Once smoothed, data is linearly interpolated to the time scale for the tip-path-plane imaging system. Therefore, the sensor histories recorded by the in-flight system (alpha-vane angle of attack and free-stream velocity) are accurate to ±50µs and the sensor histories recorded by the PPDG system (inertial velocity, inertial acceleration, and pitch angle) are accurate to ±1 ms.

6.2 Data

Once synchronized and mapped to a common time scale, the data could be evaluated. The answers to two fundamental questions are answered in this section:

1. Was the measurement strategy for tracking the tip-path-plane angle defined in Chapter 3 effective?

2. Did the data support the first order principles derived in Chapter 2?

The angle of the reference axis with respect to the free-stream velocity as measured by the alpha vane on the air data boom, α_0, and the angle of the tip-path-plane with respect to the reference axis as measured by the imaging system, α_1, for various flight conditions are shown in Figure 6.1. The abscissa axis in this plot is the theoretical tip-path-plane angle based on the drag-to-weight ratio, flight path angle, and acceleration and the ordinate axis is the measured value for each of the two measurement devices.

$$-\left(\frac{D_f}{W}+\gamma+\frac{1}{g}\frac{dV}{dt}\right) \text{ (deg)}$$
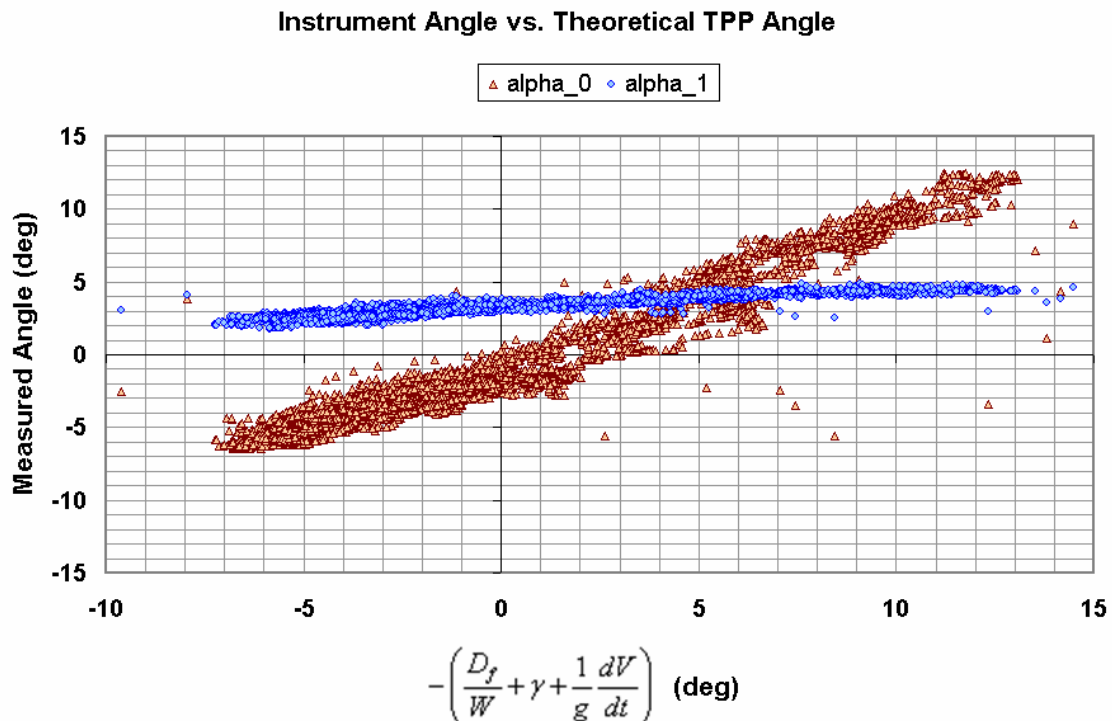
Figure 6.1: Measurements of α_0 and α_1.

Two major observations can be made from Figure 6.1. First, the range of angle deflection of the blade relative to the reference axis (~3°) was small compared to the range of the free-stream velocity with respect to the same axis (~20°). Second, the standard deviation for the angle measured by the camera (0.21°) was also smaller than the standard deviation of the wind-vane measured data (1.04°). These variations are likely the result of real-world flight testing where the attitude of the aircraft cannot be maintained perfectly due to turbulence and inevitable pilot adjustments. A typical example of this variation is shown in Figure 6.2. Notice that during the maneuver, aircraft pitch fluctuations coincided with variations in the respective α_0 and α_1 measurements even though the drag-to-weight ratio, flight path angle, and acceleration were held constant.
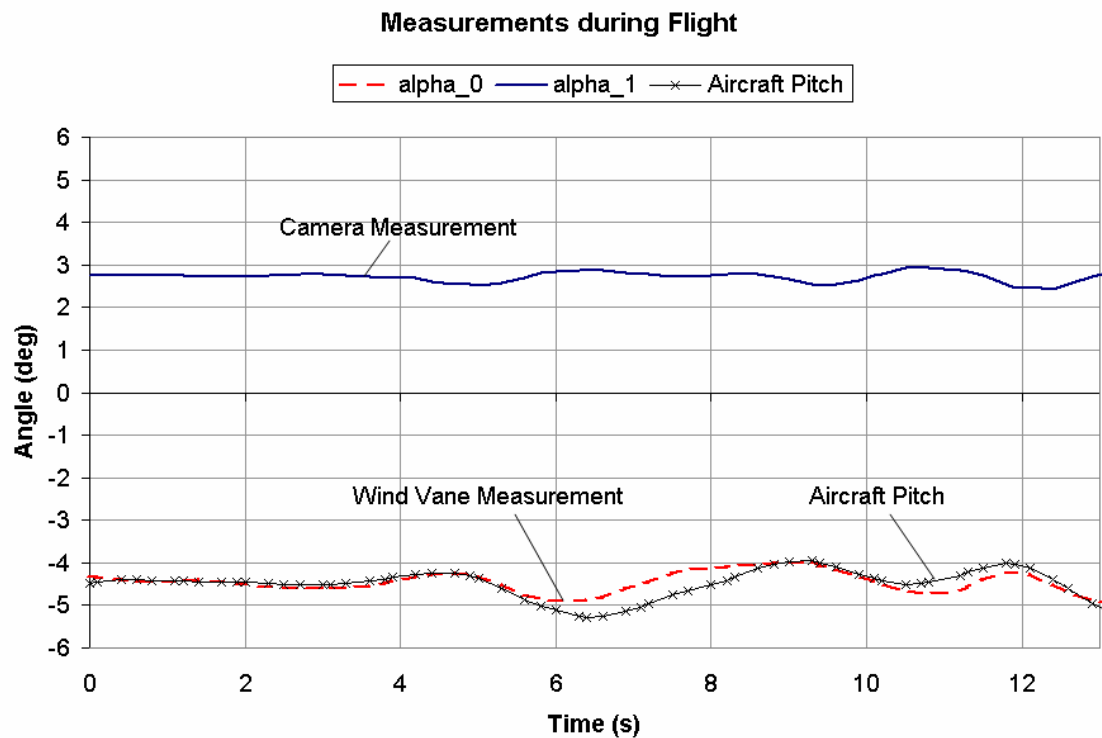
Figure 6.2: Variation in instrument measurements for a typical maneuver.

The measured tip-path-plane angle with respect to the free stream velocity is plotted against the theoretical tip-path-plane angle in Figure 6.3. When a trend line is fit to the data, the slope of the trend matches theory, but a 2.5° offset is present. This offset is most likely the result of a discrepancy between the reference axis used in the tip-path-plane imaging system and the reference axis used by the inertial measurement system and error in quantifying the equivalent flat-plate that appears in the drag-to-weight ratio term. Overall, the standard deviation of the combined data is 1.06°.

It should be noted that during testing, the helicopter was fitted with a spray-rig that had been modified to accommodate microphones for acoustic testing purposes. This rig added a substantial amount of drag to the vehicle and had a large influence on the equivalent flat plate area. Furthermore, the equivalent flat plate area was assumed constant regardless of helicopter attitude. This assumption made accurate drag-to-weight ratio estimates difficult to obtain.
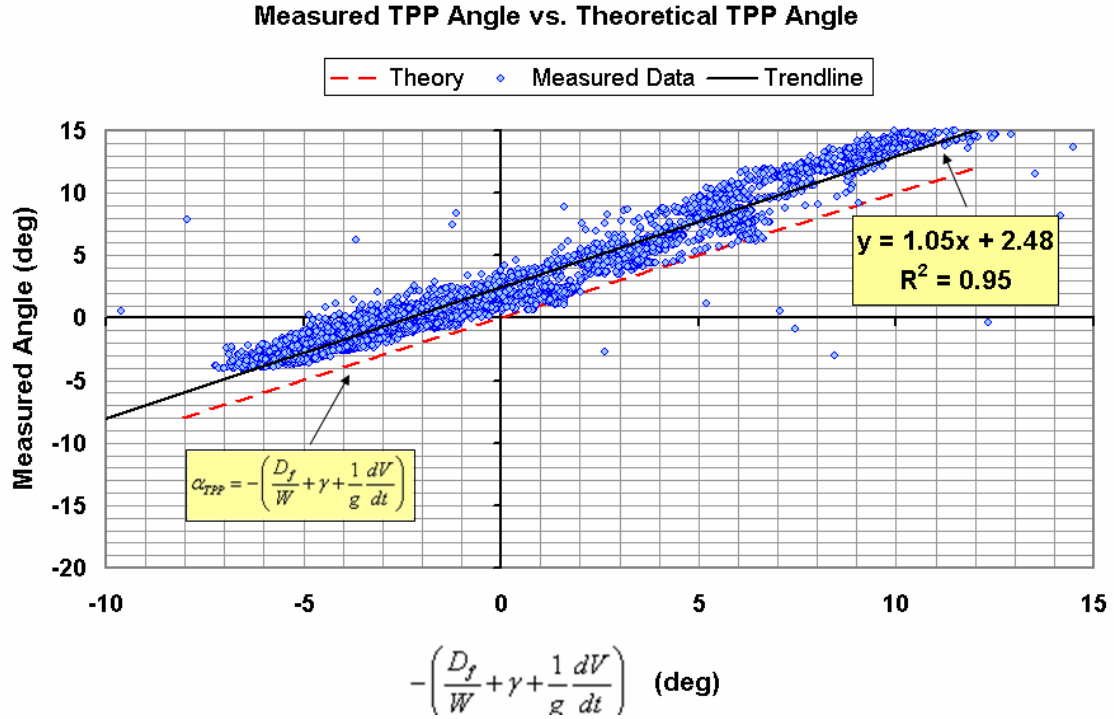
Figure 6.3: Measured tip-path-plane angle versus theoretical tip-path-plane angle.

Next, the recorded data was used to verify the first-order principles that were derived in Chapter 2 – that the tip-path-plane angle is a function of the drag-to-weight ratio, flight path angle, and acceleration:

$$\alpha_{TPP} \approx -\left(\frac{D_f}{W} + \gamma + \frac{1}{g} \frac{dV}{dt} \right)$$

(2.30)

Consider the drag-to-weight ratio term. Since the fuselage drag is proportional to the *square* of the velocity, if the flight-path angle and acceleration are fixed, the tip-path-plane angle should decrease with the square of the free-stream velocity. This trend is visible in Figure 6.4 for steady level flight. Again, the scattering is due to variations in the flight condition and uncertainties in the equivalent flat plate area.

Tip-Path Plane Angle by Velocity

$$\alpha_{TPP} = -\frac{\rho f}{2W}V_\infty^2 = -\left(0.0008\,{}^{deg}\!/_{knots^2}\right)V_\infty^2$$

$$\alpha_{TPP} :: [\text{deg}]$$

$$V_\infty :: [\text{knots}]$$

$$y = -0.0008x^2 + 1.52$$

Figure 6.4: Tip-path-plane angle vs. velocity.

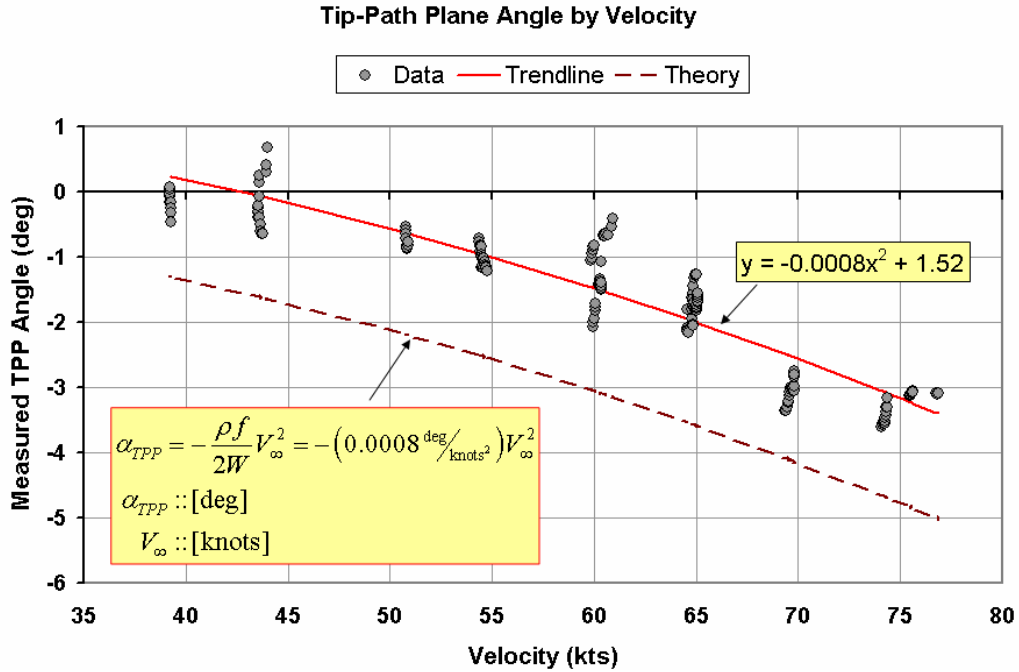The theoretical relationship between the measured tip-path-plane angle and the velocity is also plotted in Figure 6.4. If the flight path angle and acceleration are zero, the theoretical coefficient in front of the velocity squared term should be -0.0008 deg/knots^2. Indeed, the magnitude of the coefficient for the trend line matches the theoretical value. However, the constant 1.5° offset is the result of the discrepancy between the reference axis used by the tip-path-plane imaging system and the inertial measurement system.

Next consider the flight-path angle term. From the fundamental equation, if the velocity and acceleration are fixed, the measured tip-path-plane angle should decrease linearly with increasing flight-path angles. The relationship for steady level flight at 65 knots is provided in Figure 6.5. along with the theoretical tip-path-plane angle. Note that the slope of the trend line fit to the data agrees well with theory. The offset is due to the previously mentioned measurement errors.

Tip-Path Plane Angle by Flight Path Angle
(Velocity ~65 kts)

$$\alpha_{TPP} = -\left(\frac{\rho f}{2W}V_\infty^2 + \gamma\right) = -\gamma - 3.58$$

$$\alpha_{TPP} :: [\text{deg}]$$

$$\gamma :: [\text{deg}]$$

y = -1.09x - 0.84
$R^2 = 0.98$
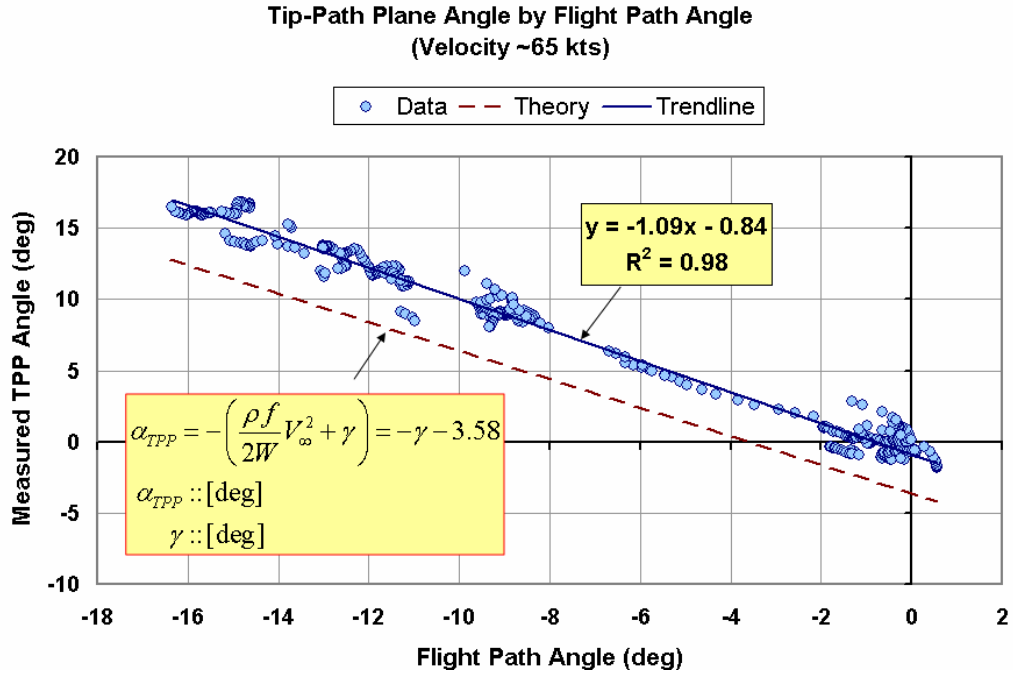
Figure 6.5: Tip-path-plane angle vs. flight path angle.

Lastly, the final term suggests that for a fixed flight path angle and velocity, the tip-path-plane angle should decrease linearly with increasing acceleration. A level-flight deceleration cases with an initial velocity of 60 knots is plotted in Figure 6.4 along with the theoretical tip-path-plane angle. Trend lines fit to the data verify the linear relationship between the acceleration and the measured tip-path-plane angle but due to the difficult nature of marinating a constant acceleration during flight, the slope of the trend line does not perfectly match the theoretical curve. Again, the offset is due to the error in estimating the equivalent flat plate area and bias between the instrumentation reference axes.
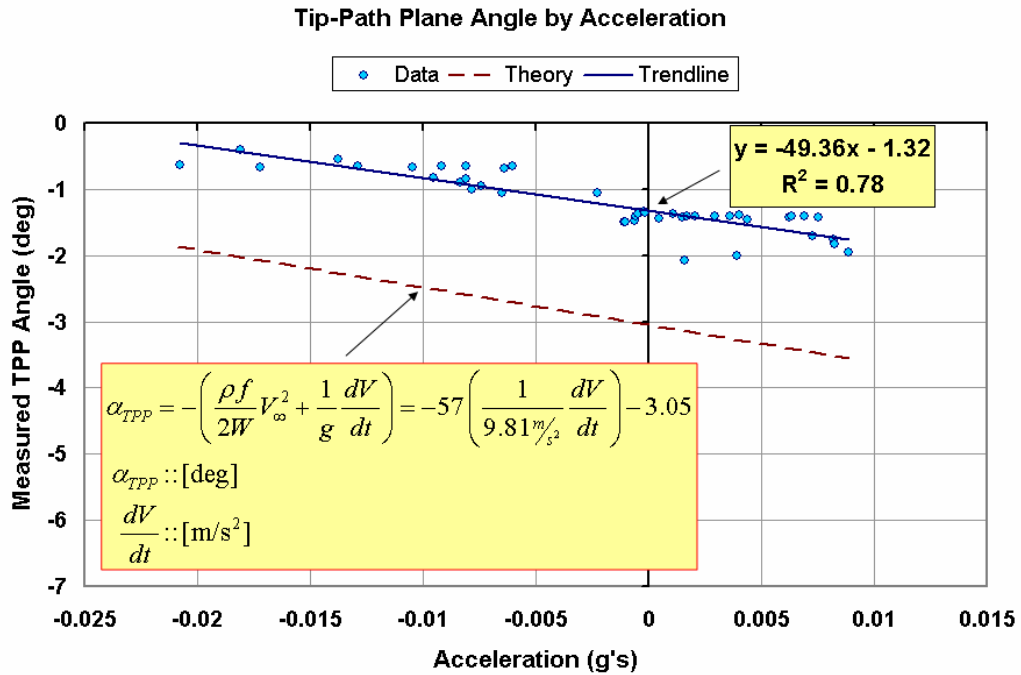
Figure 6.6: Measured tip-path-plane angle vs. acceleration.

6.3 Error Analysis

There were two primary sources of error in this evaluation. The first, measurement error, limited the overall accuracy of the imaging system to correctly track the tip-path-plane. The second, the pilot's ability to maintain the flight condition, was essential to ensuring the steady state assumption. These two sources of error are further examined below.

6.3.1 Measurement Error

Measurement errors for the commercial-off-the-shelf systems were described in Chapter 4. However, since the system that measured the tip-path-plane relative to the reference axis was a custom system, the measurement error is a function of the optics, the tracking algorithm, and the calibration technique.

Each camera has a resolution of 1280 pixels in the plane parallel to the laser image projection. The field of view along this plane is 29.9° based on the camera specifications[20]. Therefore, the location of an object in a pixel bin is accurate to within 0.0239° if addressed in the middle bins (address 640 or 641) reducing to within 0.0224° if addressed in one of the extreme bins (address 1 or 1280).
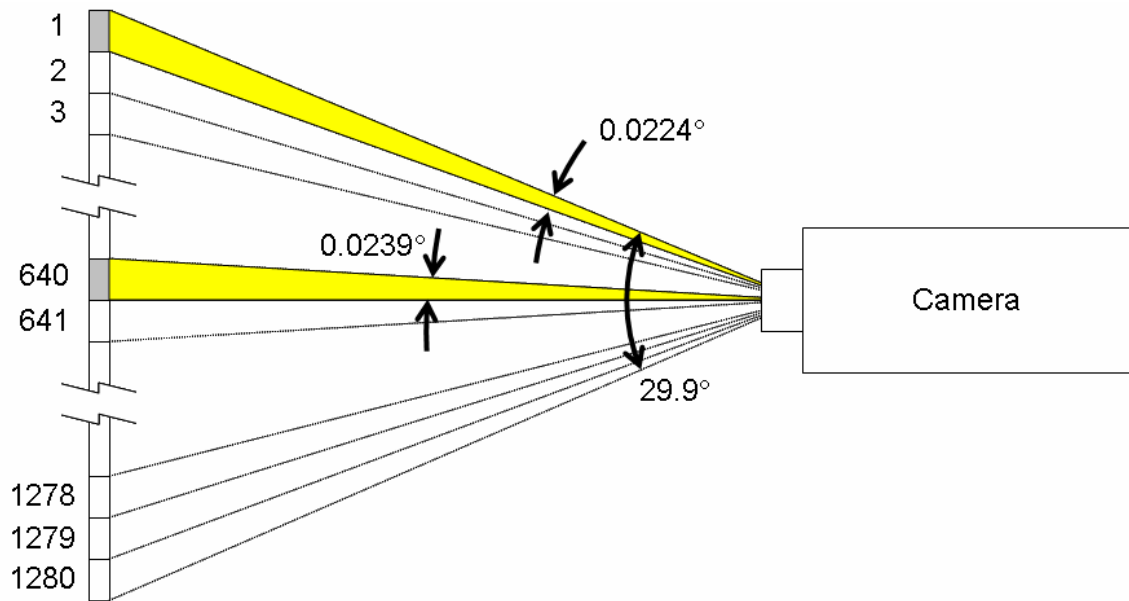
Figure 6.7: Camera measurement error.

The next source of measurement error deals with a trigonometric approximation used in the tracking algorithm. To free computational resources, the algorithm assumes a linear correlation between the pixel address and the blade angle relative to the camera. Figure 6.8 illustrates the error of this approximation as the tip target shifts from the center of the image. At the extreme regions, this error could be as much as 0.17°. However, in practice the range of the blade motion was quite limited and the error tended to stay within 0.01°.
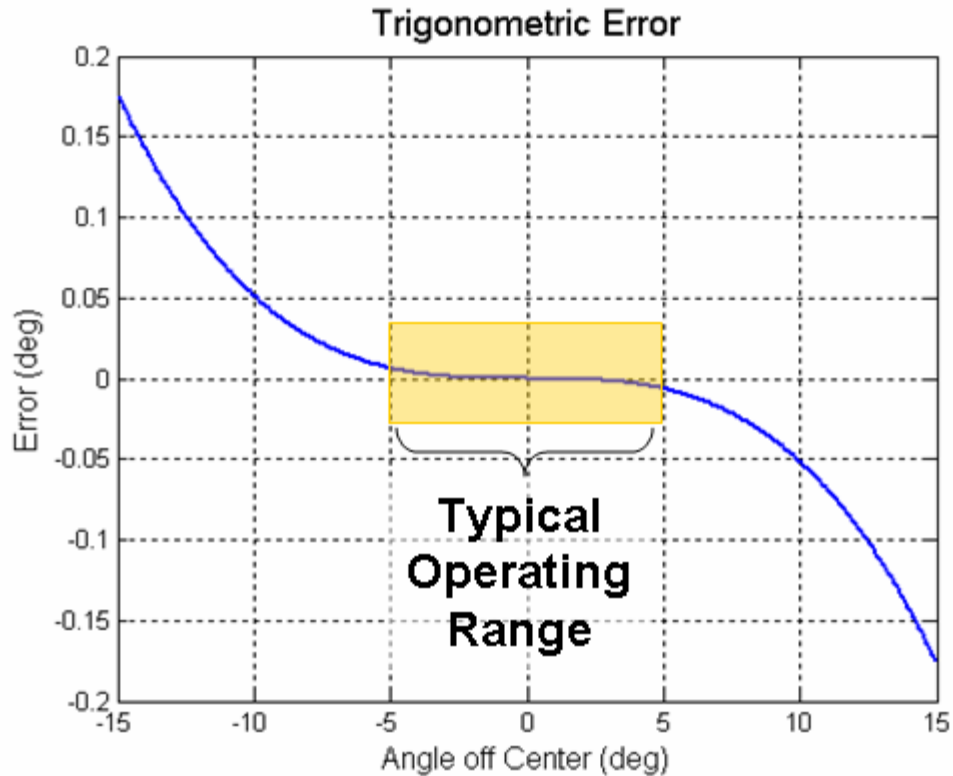
Figure 6.8: Trigonometric approximation error.

The final source of measurement error resulted from the calibration process. When calibrating, the blade position angle was measured using an inclinometer with an accuracy of ±0.1°. This constituted the largest source of measurement error.

When all three sources are combined, the blade measurement error was typically within ±0.133°, or ±0.417" on the Bell 206B helicopter. Much of this error could be removed by using alternative calibration procedures.

6.3.2   Sensitivity to Flight Condition

As mentioned previously in Section 6.2, the scattering is most likely attributed to variations in flight condition. To assess this hypothesis, a section of data was isolated where the pilot maintained a nearly perfect condition. The measurements, shown in

Figure 6.9, show that if the pilot held velocity, flight path angle, and acceleration constant, then the theoretical tip-path-plane angle varied very little. For the same flight condition, the measurements made by the camera system and wind vane also varied little and the measured tip-path-plane matched the same behavior as the predicted value. Notice that the offset mentioned previously between the predicted and measured tip-path-plane angle is still present.
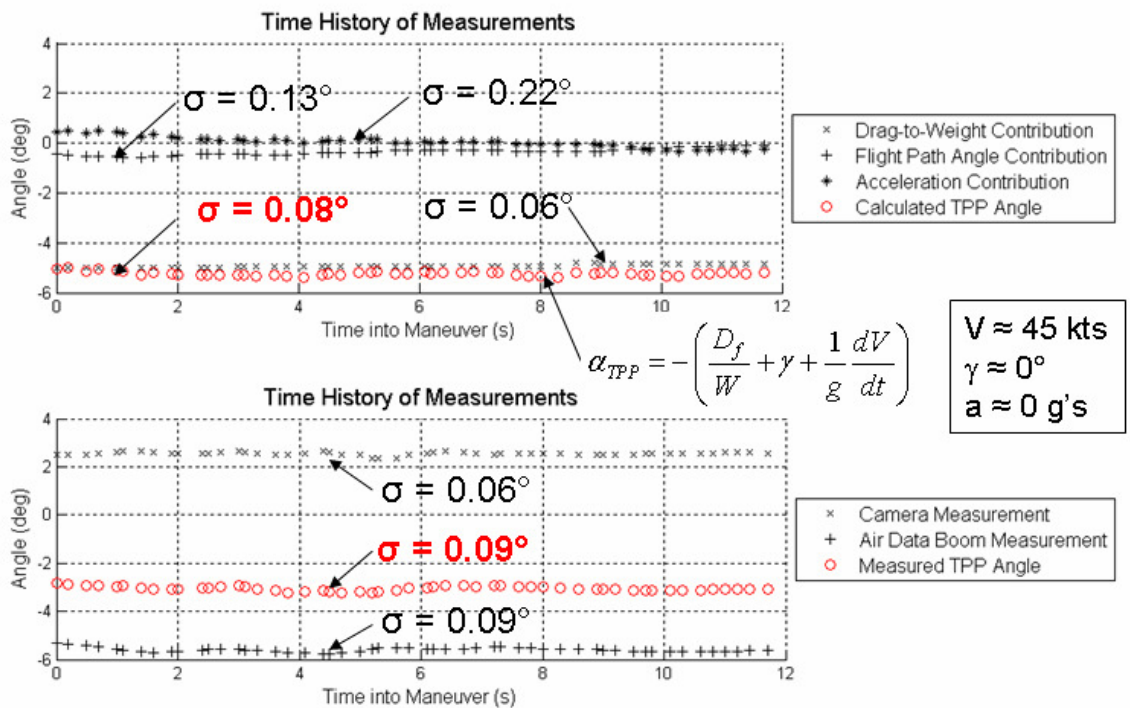

Figure 6.9: Predicted tip-path-plane angle (top) and measured tip-path-plane angle (bottom) for a truly steady state maneuver.

Chapter 7: Summary and Conclusions

This research documents the development of a longitudinal tip-path-plane imaging system that can be used for the purpose of monitoring the inflow state of a helicopter in flight.

7.1   Conclusions

- **An optics-based longitudinal tip-path-plane tracking system was successfully demonstrated in flight on a Bell 206B helicopter**. Such a system can ideally be used to monitor the inflow state of the helicopter and predict the intensity of the blade-vortex interaction noise.

    o **Using commercial-off-the-shelf components, a camera system was developed that takes simultaneous images of the rotor blades each revolution.** Unlike systems used for tracking and balancing, this system reports the longitudinal angle of the tip-path-plane relative to a fuselage reference axis. Furthermore, this system requires no major alterations to the rotor blades – just the addition reflective tip targets similar to those used for track and balancing applications. The overall accuracy of the tracking system is ±0.13° - largely limited by the instrument used during the calibration process. The standard deviation of measurements with this system is within 0.21°.

    o **A unique differencing algorithm is used to process the images and localize the blade tips**. Though the optics were selected to maximize the intensity of the illuminated tip target over the background ambient light,

there are instances when artifacts in the background are brighter than the target. To remedy this, a differencing algorithm was developed that interrogates regions where the tip target must be illuminated and compares the image to regions where the tip target cannot be illuminated. The result is a system that can localize the illuminated tip target under a variety of ambient light conditions provided that the image has not been saturated by sunlight (i.e. when the incidence angle between the camera and the sun is typically less than 7°).

- o **An air data boom was also integrated to track the longitudinal component of the angle of attack between the free-stream velocity and the reference axis used by the camera system.** Though this component proved highly susceptible to variations in flight condition, but when the pilot maintained a steady state condition with little variation in airspeed, flight path angle, or acceleration, the angle of attack measurement similarly remained steady. This variation could be mitigated by using an inertial measurement system to obtain the free-stream velocity angle.

- **The Q-SAM theory was validated for longitudinal flight maneuvers.** When flight path angle and acceleration were held constant, the longitudinal tip-path-plane angle varied with the square of the airspeed of the helicopter. When airspeed and acceleration were held constant, the longitudinal tip-path-plane angle varied linearly with the flight path angle. And when the airspeed and flight path angle were held constant, the longitudinal tip-path-plane angle varied linearly

with the acceleration. These relations were in agreement with the model derived by solving the longitudinal force balance along the wind axis.

7.2   Future Work

Though the longitudinal tip-path-plane imaging system proved highly successful, many areas can be addressed for future improvement.

- **Calibration procedures need to be improved.** Though the accuracy of the camera measurement is within $0.13°$, $0.10°$ of that is due to the calibration technique which employs an inclinometer. To mitigate this, blade position should be calibrated using an alternate measurement technique. For instance, the altitude of the blade tips could be measured using range finders.

- **Improved measurement of equivalent flat plate area.** Errors in the estimation of the equivalent flat plate area yield a bias in the drag-to-weight ratio term of the theoretical longitudinal tip-path-plane angle. There are two ways to address the issue. First, additional techniques such as CFD or wind-tunnel testing could be used to obtain better estimates of the equivalent flat plate area based on the attitude of the helicopter. Secondly, the derived force balance theory could be used in conjunction with the measurements made by the tip-path-plane imaging system to back out the equivalent flat plate area for steady state maneuvers in no-wind conditions. Either would effectively remove the bias between the theoretical and the measured longitudinal tip-path-plane angle witnessed in the results section.

- **Expansion to track the full tip-path-plane.** The current system only monitors the longitudinal component of the tip-path-plane and would not provide any

insight to the inflow state of the helicopter during lateral maneuvers. However, by installing an additional camera, the entire plane of the rotor could be tracked. It would also be advantageous to install a four-camera system. That way, even if one of the cameras is pointed directly at the sun and is unable to track the blade tips, the tip-path-plane could still be tracked from the remaining three cameras via a voting process.

- **Correlation of measured data with acoustic measurements.** The 2006 flight test that evaluated the tip-path-plane imaging system also recorded the acoustic signature of the aircraft during the flown maneuvers. Thus, it would be advantageous to correlate the measured tip-path-plane angle with the intensity of the blade-vortex interaction noise. This is important to validate the relationships between the tip-path-plane angle, inflow, and BVI radiation. Additional testing should also be performed in smooth, moderate, and rough air to see how the radiated noise correlates with inflow in flight conditions that are not ideal.

- **Incorporation into real-time displays and BVI noise indicator.** Since the blade tracking is performed in real time, it would be advantageous to install a real time display that presents the information to the pilot. By calculating the inflow state of the helicopter based on the principles of momentum theory, the pilot could be warned when they are flying a maneuver known to produce large levels of BVI noise. This display could also suggest alternate flight maneuvers to avoid zero-inflow conditions where BVI is most intense.

Bibliography

1.   Brentner, K. S., and Farassat, F., "Modeling Aerodynamically Generated Sound of Helicopter Rotors," Progress in Aerospace Sciences, Vol 39, Nos. 2-3. February-April 2003.

2.   Schmitz, F. H., "Reduction of Blade-Vortex Interaction (BVI) Noise Through X Force Control," Journal of the American Helicopter Society, Vol 43, No. 1, January 1998.

3.   Schmitz, F. H., Gopalan, G., Sim, B. W., "Flight Path Management and Control Methodology to Reduce Helicopter Blade-Vortex Interaction (BVI) Noise," Journal of Aircraft, Vol 39, No. 2, March-April 2002.

4.   Gopalan, G., Schmitz, F. H., Sim, B. W., "Flight Path Control Methodology of Helicopter Blade-Vortex Interaction (BVI) Noise in the Presence of Wind." Accepted for publication in the Journal of the American Helicopter Society.

5.   Sim, B. W., Beasman, T., Schmitz, F. H., Gopalan, G., "In-Flight Blade-Vortex Interaction (BVI) Noise Measurements Using a Boom-Mounted Microphone Array." American Helicopter Society Annual Forum. American Helicopter Society. Baltimore, MD. June 2004.

6.   Sim, B. W., Schmitz, F. H., Beasman, T., "Blade-Vortex Interaction (BVI) Noise of Helicopters Operating in Horizontal Wind Shear." American Helicopter Society 61st Annual Forum. American Helicopter Society. Grapevine TX. June 2005.

7.   Leishman, G. "Principles of Helicopter Aerodynamics," 2nd ed. Cambridge: Cambridge University Press. Cambridge, 2006.

8.   Department of the Army. "Fundamentals of Rotor and Power Train Maintenance – Techniques and Procedures." (FM 1-514). Washington, DC. Apr. 1991.

9.   Talbot, Richard. 1989. "Detector Device for a Blade Tracking System Having Two Sensors." U.S. Patent 4,812,643.

10. Department of the Navy. "Aviation Structural Mechanic (H & S) 3 & 2." (NAVEDTRA 14018). Naval Education and Training Professional Development and Technology Center, 1993.

11. Heller, Arnie. "Exploring he Ultrawideband." Science & Technology Review. May 2007.

12. Miles Griot. "The Practical Application of Light." Vol 10. 13.1-13.54.

13. CVI Laser, LLC. "Optical Components and Assemblies." 2005. 286-332.

14. ThorLabs. "Tools of the Trade". Vol 18.

15. Edmund Optics – America. "Optics and Optical Instruments Catalog." NO71C. 2007.

16. Omega Optical. "Online catalog." <https://www.omegafilters.com>. 2007.

17. U.S. Laser Corporation. "Online catalog." <http://www.uslasercorp.com>. 2007.

18. CrystaLaser. "Online catalog." <http://www.crystalaser.com>. 2007.

19. ASTM International. "Standard Tables for Reference Solar Spectral Irradiances: Direct Normal and Hemispherical on 37° Tilted Surface." (ADJG0173) ASTM Int'l. Apr. 2003.

20. Sony Corporation. "Digital Video Camera Module Technical Manual: XCD-SX910CR/X710CR, XCD-SX910UV, XCD-SX910/X710." (A-BS3-100-13(1)). Sony Corporation. 2003.